

Improved representation of clouds in the atmospheric component LMDZ6A of the IPSL Earth system model IPSL-CM6A

Jean-Baptiste Madeleine¹, Frédéric Hourdin¹, Jean-Yves Grandpeix¹,
Catherine Rio², Jean-Louis Dufresne¹, Etienne Vignon⁴, Olivier Boucher⁵,
Dimitra Konsta³, Frédérique Cheruy¹, Ionela Musat¹, Abderrahmane
Idelkadi¹, Laurent Fairhead¹, Ehouarn Millour¹, Marie-Pierre Lefebvre², Lidia
Mellul¹, Nicolas Rochetin¹, Florentin Lemonnier¹, Ludovic Touzé-Peiffer¹, and
Marine Bonazzola¹

¹Sorbonne Université, Laboratoire de Météorologie Dynamique/Institut Pierre-Simon Laplace
(LMD/IPSL), Centre National de la Recherche Scientifique (CNRS), École Polytechnique, École Normale
Supérieure (ENS), PSL Université, Institut Polytechnique de Paris, Campus Pierre et Marie Curie, BC99,
4 place Jussieu, Paris, France

²Centre national des recherches météorologiques (CNRM), Université de Toulouse, Météo-France, CNRS,
Toulouse, France

³Laboratory of Climatology and Atmospheric Environment (LACAE), National and Kapodistrian
University of Athens (NKUA), Athens, Greece

⁴Environmental Remote Sensing Laboratory (LTE), École Polytechnique Fédérale de Lausanne (EPFL),
Lausanne, Switzerland

⁵Institut Pierre-Simon Laplace, Sorbonne Université / CNRS, Paris, France

Key Points:

- Cloud parameterizations of the LMDZ6A climate model are entirely described.
- Low- and mid-level cloud distribution and radiative effects are improved compared to LMDZ5A.
- LMDZ6A is better tuned than LMDZ5A, and knowledge of its structural deficiencies has been gained.

Abstract

The cloud parameterizations of the LMDZ6A climate model (the atmospheric component of the IPSL-CM6 Earth system model) are entirely described and the global cloud distribution and cloud radiative effects are evaluated against the CALIPSO-CloudSat and CERES observations. The cloud parameterizations in recent versions of LMDZ favor an object-oriented approach for convection, with two distinct parameterizations for shallow and deep convection, and a coupling between convection and cloud description through the specification of the subgrid scale distribution of water. Compared to the previous version of the model (LMDZ5A), LMDZ6A better represents the low-level cloud distribution in the tropical belt, and low-level cloud reflectance and cover are closer to the PARASOL and CALIPSO-GOCCP observations. Mid-level clouds, which were mostly missing in LMDZ5A, are now better represented globally. The distribution of cloud liquid and ice in mixed-phase clouds is also in better agreement with the observations. Among identified deficiencies, low-level cloud covers are too high in mid- to high-latitude regions and high-level cloud covers are biased low globally. However, the cloud global distribution is significantly improved and progress has been made in the tuning of the model, resulting in a radiative balance in close agreement with the CERES observations. Improved tuning also revealed structural biases in LMDZ6A, which are currently being addressed through a series of new physical and radiative parameterizations for the next version of LMDZ.

Plain Language Summary

This paper describes the representation of clouds in the latest version of LMDZ, which is a French atmospheric model used for climate change projections. Along with other international climate models, it serves as a basis for the IPCC (Intergovernmental Panel on Climate Change) report by contributing to the CMIP project (Climate Model Intercomparison Project). Clouds are especially important in the climate system because they reflect a lot of sunlight and also absorb and emit a lot of infrared radiation. They can either amplify or reduce the current global warming depending on their change in opacity, altitude and detailed properties. It is therefore essential to represent them accurately in climate models. The main physical equations used to compute cloud properties in LMDZ are introduced and the model results are compared to various satellite observations. It reveals that low-level and mid-level clouds

59 are in better agreement with the observations than before, but that high-level clouds
60 remain difficult to simulate realistically. Ongoing developments aimed at solving these
61 remaining deficiencies are finally described.

62 **1 Introduction**

63 On average, two thirds of the Earth’s surface is covered by clouds (King et al.,
64 2013), which are therefore of primary importance in the energy budget of the atmo-
65 sphere. Similarly, cloud response to global warming is one of the largest sources of
66 uncertainty in climate change simulations (Bony et al., 2006; Dufresne & Bony, 2008;
67 Vial et al., 2013). From the early stages of climate modeling at the “Laboratoire
68 de Météorologie Dynamique” (Sadourny, 1975; Laval et al., 1981; Sadourny & Laval,
69 1983), efforts were made to develop innovative subgrid scale parameterizations that cor-
70 rectly represents their effect (Le Treut & Li, 1991; Li, 1999). The current LMD global
71 atmospheric model, called LMDZ for its zooming capability (Hourdin et al., 2006), is
72 the atmospheric component of the Earth system model named after the French climate
73 institute where it is developed: the IPSL Climate Model or IPSL-CM. This paper de-
74 scribes the representation of clouds in the latest version of LMDZ, LMDZ6A, which
75 was used for the 6th phase of the Coupled Model Intercomparison project (CMIP6,
76 Eyring et al., 2015). The general descriptions of the IPSL-CM6A model and its atmo-
77 spheric component, LMDZ6A, can be found in this Special Collection, in two papers
78 by Boucher et al. (2020) and Hourdin et al. (2020), respectively. The two previous
79 versions of LMDZ were LMDZ5A and 5B and are described in Hourdin, Foujols, et al.
80 (2013) and Hourdin, Grandpeix, et al. (2013). Compared to version 5A, version 5B
81 was based on a profound rethinking of the parameterization of convection and clouds,
82 on which the new 6A version is built. In the present paper, we will focus on comparing
83 LMDZ5A with LMDZ6A directly, because version 5B was in many respects the proto-
84 type of version 6A. CMIP5 revealed a number of biases in LMDZ5A cloud properties
85 :

- 86 • Despite major development efforts, tropical and subtropical low-level cloud frac-
87 tions were underestimated;
- 88 • Mid-level clouds were almost inexistent;

- 89 • Large biases were found in the total cloud radiative effect over the Southern
90 Ocean;
- 91 • Low level cloud cover was underestimated and cloud reflectance was overesti-
92 mated (Konsta et al., 2016);
- 93 • The altitude of low-level clouds was too low (Konsta et al., 2016).

94 Our goal in this paper is twofold: to review the entire set of cloud parameter-
95 izations developed for LMDZ, and to present the main improvements of the newest
96 version, LMDZ6A. A particular care has been given in the LMDZ parameterizations
97 to the representation of convection, for which a deliberate choice was made to separate
98 deep and shallow convection, and which is coupled to cloud description through the
99 specification of subgrid scale distribution of total water or saturation deficit. These
100 developments have been described through a series of publications, but always focus-
101 ing on one particular aspect. The present paper provides a full description of the
102 parameterizations that control clouds in LMDZ as well as their interactions. In terms
103 of evaluation, a particular attention will be paid to the global cloud distribution and
104 its role in maintaining the global radiative balance in the model. The discussion and
105 conclusion will highlight the remaining biases and present the current development
106 efforts to address them.

107 **2 Parameterization of clouds in LMDZ6A**

108 The challenge in modeling clouds resides in the various scales of atmospheric
109 processes controlling their macro- and microphysical properties. They depend on both
110 km-scale and μm -scale processes evolving on timescales ranging from minutes to sec-
111 onds. In the last two decades, the LMDZ team worked on a set of innovative param-
112 eterizations that describe the subgrid-scale vertical motions and their connections to
113 cloud properties. Clouds in LMDZ depend on 1) turbulent mixing, shallow convection,
114 deep convection and large-scale horizontal advection, and 2) cloud statistical schemes
115 that use the physical information provided by these processes to compute their opacity
116 and the fraction of the gridbox they cover. To do so, atmospheric properties such as,
117 for example, the area covered by thermal plumes in the boundary layer or mass fluxes
118 in deep convective clouds are used to shape the subgrid scale distributions of water
119 vapor. The general approach is to represent these distributions by probability density

120 functions (PDFs) that can be unimodal or bimodal, and whose variance and asymme-
 121 try towards high humidity values increases when convective plumes bring near-surface
 122 moist air toward the drier free troposphere. Since the temperature of the gridbox is
 123 known, it is possible to derive, from these distributions, the populations of air parcels
 124 that are supersaturated, and to deduce the cloud fraction and water content.

125 All the processes occurring in a gridbox (turbulent mixing, shallow and deep
 126 convection) are called sequentially in LMDZ, as represented in Table 1. In the following
 127 sections, the different steps of this diagram will be described, from the main model
 128 prognostic variables to the final cloud fraction α_c and water content q_c^{in} , which are
 129 the two information used by the radiative transfer scheme to compute cloud radiative
 130 heating rates.

131 2.1 Evaporation

132 The first procedure of the LMDZ physical package is the evaporation of all con-
 133 densates, because most parameterizations of convection work with the total water mass
 134 mixing ratio q_t (see the early work of Betts, 1973). This does not mean that clouds
 135 are purely diagnostic. The cloud liquid and ice mixing ratios are “semi-prognostic”
 136 variables in the sense that they are advected by the dynamical core, but they are
 137 evaporated/sublimated at each timestep at the beginning of the physical package.
 138 This assumption may hold for liquid droplets whose lifetime is often smaller than the
 139 physics timestep of ~ 15 min, but can be a limitation for ice or mixed-phase clouds.
 140 This first procedure is represented in Table 1, and affects the three water phases (the
 141 water vapor, liquid water, and ice mass mixing ratios, noted q_v , q_l and q_i) as well as
 142 the potential temperature θ , through evaporative cooling. It returns the total water
 143 content q_t which is then used and updated by all the cloud parameterizations. The only
 144 other procedure affecting the prognostic variables q_l and q_i is the so-called large-scale
 145 condensation scheme, which condenses, before calling the radiative transfer scheme, all
 146 the water vapor in excess of saturation coming from the different parameterizations.

147 2.2 Local turbulent mixing

148 The first process that is accounted for is the local turbulent mixing in the bound-
 149 ary layer, which was revisited in LMDZ6A. It now includes a 1.5 order closure K-

Procedure / Subsection	Input variables	Other outputs
	○ Updated variables	
2.1. Evaporation	θ q_w q_t q_i	
	○ θ q_t ($q_l = q_i = 0$)	
2.2. Local turbulent mixing	θ q_t	
	○ θ q_t	
2.3. Deep convection	θ q_t ALE ALP	$q_c^{in,cv}$ $P_{l,i}^{cv}$ $d\theta_{dw}^{cv}$ $dq_{t,dw}^{cv}$
	○ θ q_t	
2.4. Deep convection PDF	q_t $q_c^{in,cv}$	α_c^{cv}
2.5. Cold pools (wakes)	θ q_t $d\theta_{dw}^{cv}$ $dq_{t,dw}^{cv}$	ALE^{wk} ALP^{wk} θ_{env}^{wk} $q_{t,env}^{wk}$
	○ θ q_t	
2.6. Shallow convection	θ_{env}^{wk} $q_{t,env}^{wk}$	$(s_{th}$ σ_{th} s_{env} $\sigma_{env})^{th}$ ALE^{th} ALP^{th}
	○ θ q_t	
2.7. Large-scale condensation	θ q_t $(s_{th}$ σ_{th} s_{env} $\sigma_{env})^{th}$	$q_c^{in,lsc}$ α_c^{lsc} $P_{l,i}^{lsc}$
	○ θ q_w q_t q_i	
2.8. Radiative transfer	$q_c^{in,lsc}$ α_c^{lsc} $q_c^{in,cv}$ α_c^{cv}	
	○ θ	

Table 1. Architecture of the physical package, showing all cloud-related variables. The first column gives the names of the different procedures, that are also used as subsection titles in section 2. The second column indicates the main variables used by the procedure on the left, and the prognostic variables that are updated at the end of the procedure on the right, in gray. The other useful variables computed by each procedure are given in the last column. Variables colored in blue are related to cloud properties, and are those used by the radiative transfer scheme to compute the cloud radiative effect. All the notations are given in the text and summarized in Appendix A.

150 gradient scheme and a prognostic equation for the TKE (Turbulent Kinetic Energy).
 151 The K-gradient scheme is based on the work of Yamada (1983), and was improved
 152 for stable boundary layers (Vignon et al., 2017; Cheruy et al., 2020). The total water
 153 vapor mass mixing ratio q_t is vertically mixed assuming a down-gradient Fick’s type
 154 diffusion whose intensity depends on the TKE. As is classical in climate models, the
 155 turbulence scheme includes the representation of exchanges with the surface, including
 156 the evaporation and sensible heat fluxes, which are essential to cloud formation.

157 **2.3 Deep convection**

158 The deep convection scheme of LMDZ computes heating, moistening and mo-
 159 mentum changes using a modified version of the Emanuel mass flux scheme (Emanuel,
 160 1991) to which a parameterization of cold pools was added (Grandpeix & Lafore, 2010;
 161 Grandpeix et al., 2010). Version 6A differs significantly from version 5A which was
 162 using the Emanuel scheme without the improved mixing representation (Grandpeix et
 163 al., 2004) and the various improvements described in the present section.

164 Once the turbulent mixing in the boundary layer has been computed, deep con-
 165 vection can be initiated, depending on the *ALE* (Available Lifting Energy) inherited
 166 from the previous timestep. The *ALE* can be provided by frontal lifting at the edge
 167 of cold pools or by boundary layer thermals, which are noted ALE^{wk} and ALE^{th} in
 168 Table 1, respectively. The *ALE* finally used by the deep convection scheme is the
 169 largest of the two energies. Deep convection is triggered if the *ALE* exceeds the *CIN*
 170 (Convective INhibition) and if at least one of the cumulus of the domain reaches a
 171 given threshold size and evolves into a congestus or cumulonimbus cloud. This latter
 172 process is represented by a stochastic triggering scheme (Rochetin et al., 2014) and is
 173 also a new feature of LMDZ6A. Another important new feature of version 6A is the
 174 inclusion of the latent heat exchange due to the liquid \leftrightarrow ice phase change in the deep
 175 convection scheme.

176 Once deep convection has been triggered and the cold pools have been initiated,
 177 the column is split in two separate fields: the cold pool area and its environment,
 178 each having their own temperature and humidity. Deep convection then “sees” the
 179 environment of cold pools, rather than the mean grid cell, while downdrafts fall inside
 180 the cold pool region. This so-called splitting technique is essential to maintain deep

181 convection within the grid cell. The deep convection closure is based on the *ALP*
 182 (Available Lifting Power, see Grandpeix et al., 2010), which is inherited from the
 183 previous timestep and is the sum of the *ALP* provided by the cold pools and by the
 184 thermal plumes of the boundary layer.

185 The deep convection scheme then computes the in-cloud water mass mixing ra-
 186 tio $q_c^{in,cv}$, which is the ratio of condensed water mass to *in-cloud* air mass. Note that
 187 this quantity is different from the liquid or ice mass mixing ratios within a gridbox
 188 q_l and q_i which correspond to the ratio of condensed water mass to *gridbox* air mass.
 189 It also computes the convective rainfall and snowfall $P_{l,i}^{cv}$. The precipitation mecha-
 190 nism follows Emanuel and Ivkovi-Rothman (1999): all the condensate in excess of a
 191 temperature-dependent conversion threshold is converted into large hydrometeors that
 192 will eventually fall. The precipitation efficiency (i.e. the fraction of large hydromete-
 193 ors in the total condensate) is bounded by a maximum value ep_{max} , which is usually
 194 slightly lower than 1 (see Table 2) to always keep some cloud water in the atmosphere
 195 (Bony & Emanuel, 2001). All the condensate is carried up in the updrafts till their
 196 ends, at which point the large hydrometeors fall as precipitation with a prescribed
 197 terminal velocity.

198 In our scheme, both the undiluted updrafts and the mixed drafts contribute to the
 199 in-cloud water content of deep convective clouds. The deep convective cloud fraction
 200 α_c^{cv} is computed (as explained in section 2.4) from the in-cloud water content of deep
 201 convective clouds $q_c^{in,cv}$, which is itself deduced from the different mass fluxes and
 202 coverage fraction of undiluted and mixed updrafts. In the case of undiluted updrafts,
 203 the coverage fraction α_a is given by $\alpha_a = M_a / (\rho w_a)$ where M_a is the mass flux density
 204 and w_a the vertical velocity. In the case of the mixed drafts, the entrained air at
 205 each level feeds cloud formation, and these clouds dissipate with a time constant τ_m .
 206 Therefore, the time evolution of the cloud water mass in a layer of thickness δz can be
 207 written as:

$$\frac{\partial}{\partial t} (\rho \alpha_m \delta z q_m) = M_t q_m - \frac{\rho \alpha_m \delta z q_m}{\tau_m}, \quad (1)$$

208 where M_t is the mass flux density of the mixed drafts and q_m its condensed water
 209 mixing ratio. The coverage fraction of mixed drafts can then be deduced from equa-
 210 tion 1 by assuming a steady-state, which gives $\alpha_m = M_t \tau_m / (\rho \delta z)$. The in-cloud water

211 content is finally calculated as a linear combination of the cloud water of the undiluted
 212 updraft and mixed drafts:

$$q_c^{in,cv} = \frac{\alpha_a q_a + \alpha_m q_m}{\alpha_a + \alpha_m}, \quad (2)$$

213 where q_a is the condensed water mixing ratio of the undiluted updraft. In equation 1,
 214 the saturated draft dissipates with a time constant τ_m of the order of 100 s.

215 This in-cloud water content $q_c^{in,cv}$ is computed for use in the radiative transfer
 216 scheme and in the deep convective cloud statistical scheme (see the next section), but
 217 it is not removed from the vapor phase or used to derive the prognostic variables q_l and
 218 q_i . At the end of the deep convection scheme, the vertical profiles of convective rainfall
 219 and snowfall $P_{t,i}^{cv}$ are returned and removed from the vapor phase, and only θ and the
 220 total water mass mixing ratio q_t are changed accordingly. The deep convection scheme
 221 also returns the change in both temperature and water content due to downdrafts $d\theta_{dw}^{cv}$
 222 and $dq_{t,dw}^{cv}$, which are later used by the cold pool scheme (see section 2.5).

233 2.4 Deep convection PDF

234 As briefly mentioned at the beginning of this section, the cloud statistical schemes
 235 used in LMDZ are tightly connected to the information provided by the shallow and
 236 deep convection schemes. Such statistical schemes rely on a PDF describing the subgrid
 237 scale distribution of water vapor or saturation deficit. In the case of deep convection,
 238 the total mass mixing ratio of water q within the gridbox is assumed to be a random
 239 variable of mean value q_t . The latter can be written as:

$$q_t = \int_0^\infty q P(q) dq. \quad (3)$$

240 The cloud mixing ratio q_l or q_i and cloud fraction α_c can then be computed as:

$$q_{l,i} = \int_{q_{sat}}^\infty (q - q_{sat}) P(q) dq, \text{ and} \quad (4)$$

$$\alpha_c = \int_{q_{sat}}^\infty P(q) dq, \quad (5)$$

231 where q_{sat} is the water vapor saturation mixing ratio at the gridbox mean tempera-
 232 ture and pressure, i.e. $q_{sat}(\bar{T}, \bar{p})$. We neglect in this case the effect of temperature
 233 heterogeneities on q_{sat} . The gridbox mean amount of both condensates and in-cloud
 234 vapor, q_{t_c} , can be written as:

$$q_{t_c} = \int_{q_{sat}}^{\infty} q P(q) dq, \text{ with} \quad (6)$$

$$q_{t_c} = q_{l,i} + \alpha_c q_{sat}. \quad (7)$$

235 In this context, the in-cloud water content q_c^{in} is given by :

$$q_c^{in} = \frac{\int_{q_{sat}}^{\infty} (q - q_{sat}) P(q) dq}{\int_{q_{sat}}^{\infty} P(q) dq} = \frac{q_{l,i}}{\alpha_c}. \quad (8)$$

236 The deep convection scheme provides the in-cloud water content $q_c^{in,cv}$, as de-
 237 scribed in section 2.3. Therefore, the three free parameters of a lognormal PDF are
 238 then deduced from equations 3 and 8 by an inverse procedure, assuming that the PDF
 239 equals zero for $q = 0$ (Bony & Emanuel, 2001, Appendix A). The PDF is then used to
 240 compute α_c^{cv} , which is later used, together with $q_c^{in,cv}$, by the radiative transfer scheme
 241 (see Table 1).

242 2.5 Cold pools (wakes)

243 Density currents are outflows of evaporatively cooled downdrafts generated in
 244 thunderstorms and larger convective systems. They result in surface cold pools that
 245 inhibit convection locally on the one hand, but favor new convective zones at their
 246 edges on the other hand. Therefore, they play an important role in the life cycle of
 247 convective systems. Their representation is a new feature of LMDZ6A. To account
 248 for this process, the deep convection scheme assumes that a fraction of precipitation
 249 (15% above cloud base and 100% below) falls outside the cloud and evaporate to
 250 form precipitating downdrafts. The cold pool scheme then uses the change in both
 251 temperature and water content due to these downdrafts $d\theta_{dw}^{cv}$ and $dq_{t,dw}^{cv}$. As explained
 252 earlier, we use a splitting technique so that cold pools can have their own temperature
 253 and humidity. The cold pool scheme also derives its own *ALE* and *ALP* quantities that
 254 will be later used, at the next timestep, by the deep convection scheme for its triggering
 255 and closure (Grandpeix et al., 2010). Density currents affect clouds indirectly in two

256 ways. First, they redistribute heat and water vapor vertically. Second, they play a
 257 role, via the term ALE^{wk} , in triggering deep convection.

258 **2.6 Shallow convection**

259 *2.6.1 Thermal plume model and shallow cumulus convection*

260 Version 6A uses a mass flux parameterization of thermals (Hourdin et al., 2002)
 261 instead of using a counter-gradient term in the vertical derivative of potential temper-
 262 ature and a dry convective adjustment as was the case in version 5A (Hourdin, Foujols,
 263 et al., 2013). This thermal plume model was extended to the representation of shallow
 264 cumulus convection by Rio and Hourdin (2008). Conceptually, this model represents
 265 two subgrid scale objects: a given coverage fraction of thermals, and their environ-
 266 ment. The splitting technique mentioned in the previous section is also applied to the
 267 shallow convection scheme and thermals develop outside the cold pool region and in
 268 the same environment as the convective updrafts, i.e. in a more unstable environment
 269 than that of the mean atmospheric grid cell. To do so, the potential temperature and
 270 total water content outside the cold pool region (θ_{env}^{wk} and $q_{t,env}^{wk}$ in Table 1) are used as
 271 inputs of the shallow convection scheme, thereby improving the buoyancy calculations
 272 and thermals development. In LMDZ6A, the thermal plume model was also improved
 273 by changing the detrainment formulation to better represent the transition from stra-
 274 tocumulus to cumulus clouds. This was done by using in the buoyancy formulation the
 275 difference in virtual potential temperature between the updraft and the environment
 276 at two different vertical levels, instead of computing the temperature difference on a
 277 same level. This method significantly improved the representation of clouds in regions
 278 of subsidence (for more detail, see Hourdin et al., 2019).

279 *2.6.2 Statistical cloud scheme*

280 The shallow convection scheme is tightly connected to a statistical cloud scheme
 281 that uses a bi-Gaussian distribution Q of the saturation deficit s (Jam et al., 2013).
 282 The parameters required to compute the bi-Gaussian distribution are given by the
 283 thermal plume scheme and provided to the so-called large-scale condensation scheme
 284 described in the next section. In order to partly account for subgrid scale tempera-
 285 ture fluctuations, each Gaussian distribution is characterized by the mean saturation

286 deficit and standard deviation of the thermal plume (s_{th} and σ_{th}) and its environment
 287 (s_{env} and σ_{env}), where the environment corresponds to the main mode of the bimodal
 288 distribution. The bi-Gaussian PDF can therefore be written as:

$$Q(s) = (1 - \alpha_{th}) f(s, s_{env}, \sigma_{env}) + \alpha_{th} f(s, s_{th}, \sigma_{th}), \quad (9)$$

289 where α_{th} is the coverage fraction of thermals and f is the classical Gaussian PDF:

$$f(s, \bar{s}, \sigma_s) = \frac{1}{\sigma_s \sqrt{2\pi}} \exp\left(\frac{-(s - \bar{s})^2}{2\sigma_s^2}\right). \quad (10)$$

290 The in-cloud water content and cloud fraction can then be expressed as:

$$q_c^{in} = \int_0^\infty s Q(s) ds, \text{ and } \alpha_c = \int_0^\infty Q(s) ds. \quad (11)$$

291 The two mean saturation deficits s_{th} and s_{env} are computed automatically by
 292 the thermal plume model, and the variances are parameterized based on the coverage
 293 fraction of thermals α_{th} (see equations 7 and 8 of Jam et al., 2013). The shallow
 294 convection scheme does not remove the condensates from the prognostic total water
 295 variable at this stage, and only contributes to the mixing of q_t (see Table 1). Shallow
 296 convective cloud formation and conversion to precipitation is computed afterwards by
 297 the large-scale condensation scheme.

298 **2.7 Large-scale condensation**

299 The role of the large-scale condensation scheme is to condense the water vapor
 300 in excess of saturation coming from all the other procedures, as well as the water
 301 vapor brought to saturation by the large-scale horizontal circulation (which obviously
 302 affects q_t and θ as well). It is in charge of the final calculation of the prognostic
 303 variables q_l and q_i and rebuilds the cloud macrophysical properties q_c^{in} and α_c for
 304 further use in radiative transfer computations. It also computes the large-scale rainfall
 305 and snowfall rates P_l^{lsc} and P_i^{lsc} . Note that the term “large-scale” is a bit abusive in
 306 the sense that the cloud amounts and rainfall/snowfall rates computed by the large-
 307 scale condensation scheme include both large-scale clouds and shallow cumulus and
 308 stratocumulus clouds associated with the thermal plume model.

309 In practice, the large-scale condensation scheme computes, for each atmospheric
 310 column, the different processes using a vertical top-to-bottom loop. In this section,
 311 the current layer will be referred to as z_k , with z_{k+1} the overlying layer and z_{k-1}
 312 the underlying layer. The procedure computes all the condensed water contents in
 313 three steps: 1) it computes the reevaporation/sublimation of rain/snow coming from
 314 the overlying level z_{k+1} (simply called reevaporation hereinafter), 2) it computes the
 315 amount of clouds that forms in the gridbox at level z_k using a subgrid scale PDF
 316 and 3) it converts part of the cloud into rain/snow. These three tasks are performed
 317 sequentially in this order. No structural changes were made to this scheme between
 318 version 5A and 6A, but many existing parameterizations were improved and these
 319 adjustments will be noticed in the following subsections.

320 **2.7.1 Step 1: Reevaporation**

321 The loop starts with the reevaporation at level z_k of the rain or snow coming
 322 from level z_{k+1} . This reevaporation is based on the work by Klemp and Wilhelmson
 323 (1978) and Schlesinger et al. (1988) and can be written as:

$$\frac{\partial P_{l,i}}{\partial z} = \beta \left(1 - \frac{q_t}{q_{sat}} \right) \sqrt{P_{l,i}}, \quad (12)$$

324 where $P_{l,i}$ is the liquid or solid precipitation mass flux density in $\text{kg m}^{-2} \text{s}^{-1}$. It
 325 depends on the relative humidity q_t/q_{sat} and on a parameter called β , which is the same
 326 for rain and snow in LMDZ. Reevaporation is such that water vapor in the fraction of
 327 the gridbox below clouds does not exceed the saturation mixing ratio. In LMDZ5A,
 328 the reevaporation at level z_k is limited to $\alpha_c^{ev}(q_{sat} - q_t)$, where $\alpha_c^{ev}(z_k) = \alpha_c(z_{k+1})$,
 329 with α_c the actual cloud fraction simulated by the model (see the dashed line in Fig. 1).
 330 This means that at two levels below cloud base, α_c^{ev} is set to zero and reevaporation is
 331 no more possible. In LMDZ6A, α_c^{ev} was changed to the maximum cloud fraction found
 332 in the overlying layers and is reset back to zero only if precipitation at level z_{k+1} stops
 333 (see the solid line in Fig. 1). This method implies that reevaporation is more efficient
 334 in version 6A than in version 5A (see the shaded gray area in Fig. 1), if of course the
 335 value of the β coefficient in equation 12 is unchanged.

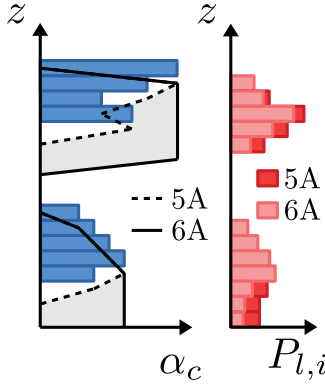


Figure 1. Diagram illustrating the two ways of computing α_c^{ev} in the rain/snow reevaporation scheme (see section 2.7). Blue and red bars show the actual cloud fraction α_c and precipitation flux density $P_{l,i}$ simulated by the model, respectively. The dashed and solid lines show the cloud fraction α_c^{ev} used to compute the maximum amount of reevaporated rain/snow in LMDZ5A and LMDZ6A.

2.7.2 Step 2: Cloud formation

Cloud formation comes next, and the computation of the amount of condensates differs whether shallow convection is active in the gridbox or not. If shallow convection is active, cloud amount and fraction are computed using the bi-Gaussian PDF described in section 2.6. To do so, it uses the mean saturation deficits (s_{th} , s_{env}) and standard deviations (σ_{th} , σ_{env}) computed by the shallow convection scheme (Table 1). Otherwise, outside the grid cells where shallow convection is active, $q_c^{in,lsc}$ and α_c^{lsc} are computed using a generalized lognormal PDF whose standard deviation σ is computed as $\sigma = \xi q_t$. ξ is a function of pressure that has changed through the different versions of the model, as shown in Fig. 2. In all versions, ξ is chosen so as to increase from the bottom of the troposphere to the top. Indeed, in the low and middle troposphere, the shallow convection scheme already computes the subgrid scale water distributions and the large-scale standard deviation σ is therefore kept close to zero. In the case where the shallow convection scheme is not active, the standard deviation σ being close to zero, the scheme is almost equivalent to an “all-or-nothing” cloud scheme. The variance of the lognormal PDF in the lower and middle troposphere was set to a higher value in LMDZ5A than in LMDZ6A (using the ξ parameter represented in Fig. 2) because the bi-Gaussian PDF was not implemented at the time and shallow convective clouds had to be represented by the lognormal PDF. In LMDZ6A, this be-

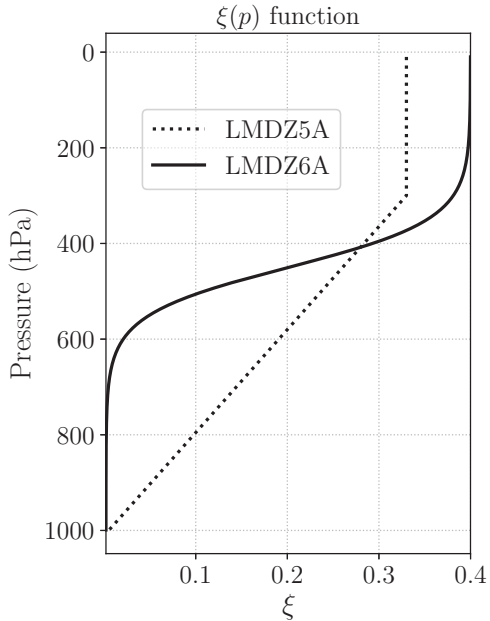


Figure 2. $\xi(p)$ profiles used in the two versions of LMDZ. ξ is used to impose the standard deviation σ of the large-scale cloud PDF, with $\sigma = \xi q_t$. The asymptotic value in the upper troposphere, noted ξ_{300} , is a tuning parameter.

355 comes useless and the variance of the lognormal PDF is strongly reduced in the lower
 356 and middle troposphere to let the bi-Gaussian PDF of the shallow convection scheme
 357 do the calculation. In the high troposphere, ξ increases to reach a maximum value
 358 ξ_{300} , which is used as a tuning coefficient. It exerts a strong control on the upper
 359 troposphere relative humidity and cloud cover (see section 3 of Hourdin, Grandpeix,
 360 et al., 2013).

361 Once $q_c^{in,lsc}$ and α_c^{lsc} are computed, the cloud phase is distributed among liquid
 362 droplets and ice crystals according to temperature, resulting in some of the liquid
 363 droplets to be supercooled. The fraction of cloud water in the liquid phase x_{liq} is
 364 computed as:

$$x_{liq} = \left(\frac{T - T_{min}}{T_{max} - T_{min}} \right)^n, \quad (13)$$

365 where T_{min} , T_{max} and n were set in version 6A to -30°C , 0°C and 0.5 respectively. As
 366 can be seen in Fig. 3, the proportion of supercooled droplets was increased in LMDZ6A

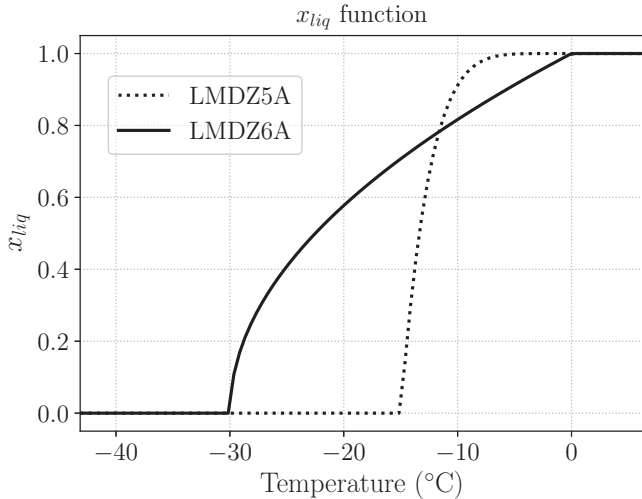


Figure 3. Liquid fraction x_{liq} as a function of temperature used in versions 5A and 6A of LMDZ.

367 to be more consistent with the most recent satellite observations (Doutriaux-Boucher
 368 & Quaas, 2004; Cesana & Chepfer, 2013; Choi et al., 2014; Cesana et al., 2015).

369 **2.7.3 Step 3: Autoconversion**

370 Part of the cloud water is converted to precipitation, depending on cloud phase.
 371 For liquid clouds, this corresponds to a sink term that can be written as:

$$\frac{dq_l}{dt} = -\frac{q_l}{\tau_{conv}} \left(1 - e^{-\left(\frac{q_l/\alpha_c}{q_{clw}}\right)^2} \right), \quad (14)$$

372 where τ_{conv} is an autoconversion time constant and q_{clw} is a threshold condensed water
 373 amount above which autoconversion sharply increases. Note that in equation 14, q_l is
 374 the liquid water mass mixing ratio within the gridbox, and that q_l/α_c is therefore the
 375 in-cloud liquid water content q_c^{in} . For ice clouds, the corresponding sink term follows:

$$\frac{dq_i}{dt} = \frac{1}{\rho} \frac{\partial}{\partial z} (\rho w_{iw} q_i), \quad (15)$$

376 where q_i is the water ice mass mixing ratio within the gridbox and where $w_{iw} = \gamma_{iw} w_0$.
 377 The fall velocity w_{iw} depends on γ_{iw} which is widely used as a tuning parameter
 378 of climate models (Mauritsen et al., 2012; Hourdin et al., 2017). The terminal fall

379 velocity is computed according to $w_0 = 3.29(\rho q_i)^{0.16}$ (Heymsfield, 1977; Heymsfield &
 380 Donner, 1990), and depends on the mass of cloud ice without taking into account any
 381 actual size or shape of the particles. The conversion from cloud water to liquid or solid
 382 precipitation is done using a subtime steps five times smaller than the physics timestep.
 383 It is worth adding that in both LMDZ5A and LMDZ6A, the cloud water content
 384 provided by the large-scale condensation scheme to the radiative transfer scheme is
 385 not what remains in the cloud at the end of the timestep, but a mean cloud water
 386 content over the duration of the physics timestep. Therefore, part of the cloud water
 387 that is converted to precipitation during the physics timestep is “seen” by the radiative
 388 transfer scheme.

389 In version 6A, the latent heat exchange due to the liquid \leftrightarrow ice phase change is
 390 not only implemented in the deep convection scheme (see section 2.3) but also in the
 391 large-scale condensation scheme. Moreover, when supercooled droplets are converted
 392 to precipitation, they freeze instantly, which was not the case in version 5A. When
 393 freezing, rain releases latent heat, which can potentially bring the temperature back to
 394 above freezing. If this is the case, a small amount of rain remains liquid to stay below
 395 freezing. At the end of the large-scale condensation scheme, both the water vapor
 396 content q_v and amount of condensates $q_{l,i}$ are known, as well as the in-cloud water
 397 content $q_c^{in,lsc}$ and cloud fraction α_c^{lsc} provided by either the bi-Gaussian PDF used
 398 for shallow convection or generalized lognormal PDF used for large-scale condensation.
 399 The prognostic variables are ready for advection by the dynamical core, and the cloud
 400 water contents and fractions can be used by the radiative transfer scheme for heating
 401 rate calculations.

402 2.8 Radiative transfer

403 Once the two cloud fractions α_c^{cv} and α_c^{lsc} are known, the total cloud fraction is
 404 estimated using:

$$\alpha_c = \min(\alpha_c^{cv} + \alpha_c^{lsc}, 1), \quad (16)$$

405 where α_c^{lsc} includes both the cloud fraction coming from shallow convective clouds
 406 (bi-Gaussian PDF) and large-scale clouds (lognormal PDF), and where α_c^{cv} is the

407 cloud fraction computed by the deep convection scheme. Similarly, the mean gridbox-
 408 averaged condensed water can be written as:

$$q_{rad} = q_c^{in,cv} \alpha_c^{cv} + q_c^{in,lsc} \alpha_c^{lsc}. \quad (17)$$

409 q_{rad} is used in the radiative transfer scheme to compute the optical depth and
 410 α_c is used to weight clear-sky and cloudy heating rates (precipitation is not radi-
 411 atively active in LMDZ). The radiative transfer scheme uses the maximum random
 412 overlap assumption (Morcrette & Fouquart, 1986; Hogan & Illingworth, 2000). Cloud
 413 phase is determined using equation 13. For liquid droplets, number concentration is
 414 parameterized using a modified version of Boucher and Lohmann (1995):

$$CDNC = 10^{1.3+0.2 \log(m_{aer})}, \quad (18)$$

415 where CDNC is the cloud droplet number concentration and m_{aer} the soluble aerosol
 416 mass (instead of the sulfate aerosol mass used in Boucher & Lohmann, 1995, equa-
 417 tion D). Droplet sizes are then computed following equations 2 and 4 of Boucher and
 418 Lohmann (1995). For ice crystals, particle sizes are parameterized following equation 6
 419 of Iacobellis and Somerville (2000) and vary in radius from r_{min} at $T < -81.4^\circ\text{C}$ to
 420 $61 \mu\text{m}$ at 0°C (Heymsfield, 1986), where r_{min} is a tuning parameter that varies be-
 421 tween 3.5 and $20 \mu\text{m}$. Note that aerosols have an impact on the size of the droplets,
 422 but not on the size of the ice crystals. The first indirect effect of aerosols is therefore
 423 represented through the aerosol-dependent size of the droplets only. Liquid cloud ra-
 424 diative properties follow Fouquart (1988) and Smith and Shi (1992) in the SW and
 425 LW domain, respectively. Ice cloud radiative properties both in SW and LW domains
 426 are computed according to Ebert and Curry (1992). Aerosol radiative properties are
 427 computed as described in Lurton et al. (2020). LMDZ5A uses the Fouquart and Bon-
 428 nel (1980) radiative transfer scheme in the SW (2 bands) and LW domains (Morcrette,
 429 1991), whereas LMDZ6A uses Fouquart and Bonnel (1980) only in the SW domain
 430 (and with 6 bands) and RRTM in the LW domain (Mlawer et al., 1997).

431 **2.9 Summary of the main improvements**

432 The changes affecting clouds made in version 6A compared to version 5A are
 433 therefore abundant, and can be summarized as follows :

- 434 • New scheme for local turbulent mixing (section 2.2) ;
- 435 • New shallow convection scheme based on the so-called Eddy-Diffusivity-Mass
 436 flux (EDMF) approach, coupled with the deep convection scheme; use of an
 437 improved statistical cloud scheme and bigaussian PDF of the subgrid scale dis-
 438 tribution of the saturation deficit; new detrainment formulation (section 2.6)
 439 ;
- 440 • New deep convection scheme that includes an improved mixing representation,
 441 new closure and a stochastic formulation of deep convection triggering (sec-
 442 tion 2.3) ;
- 443 • New parameterization of cold pools coupled with the deep convection scheme;
 444 splitting technique applied to the grid cell to distinguish the cold pool region
 445 from its environment, and to allow both the shallow and deep convections to
 446 develop outside the cold pool region (section 2.5);
- 447 • New vertical profile of the lognormal distribution’s variance used for large-scale
 448 clouds (Figure 2);
- 449 • Inclusion of the latent heat exchange due to the liquid \leftrightarrow ice phase change in
 450 both the deep convection and large-scale condensation schemes;
- 451 • New formulation of the subgrid scale rain reevaporation rate (Figure 1);
- 452 • New phase-partitioning in mixed-phase clouds (Figure 3);
- 453 • New radiative transfer scheme (section 2.8).

454 **2.10 Lessons learned from the development of LMDZ6A**

455 ***2.10.1 Pros and cons of a multi-object framework***

456 One of the most important aspects of LMDZ6A is the interplay between the
 457 different cloud parameterizations, i.e. the shallow convection scheme, the deep con-
 458 vection scheme, and the so-called large-scale condensation scheme. The deep con-
 459 vection scheme forms a set of interconnected parameterizations that includes mixing,
 460 microphysics and thermodynamics. The representation of shallow convective clouds

461 comes from two parameterizations, the thermal plume model and the large-scale con-
462 densation scheme. The thermal plume model transfers water from the surface to the
463 cloud layer and provides the parameters of the subgrid scale bi-Gaussian water distri-
464 bution. The large-scale condensation scheme handles cloud formation and computes
465 the reevaporation and autoconversion processes inside this newly formed cloud. This
466 whole framework allows us to split into pieces complex processes and gradually link
467 them together. It also enables the coupling between the different parameterizations,
468 for example the deep convection triggering by thermals and cold pools (for more con-
469 text on the state of the art of deep convection schemes, see Rio et al., 2019). However,
470 each scheme provides its own cloud PDF, and ensuring a smooth transition between
471 the different cloud PDFs is sometimes a difficult task.

472 *2.10.2 Importance of splitting the grid cell in two regions*

473 One key technical step was also distinguishing temperature and humidity inside
474 and outside the cold pool region in both the shallow and deep convection schemes, so
475 that both schemes run outside the cold pool region, in a more unstable environment
476 than that of the mean atmospheric column. In version 6A, both the thermal plumes
477 and the deep convective updrafts thus develop in a same environment of given temper-
478 ature and humidity, instead of using the mean grid-cell values. Applying this splitting
479 technique not only to the deep convection scheme (as was the case in some intermediate
480 versions of the model) but also to the thermal plume model led to a strengthening of
481 shallow convection relative to deep convection, and resulted in a major improvement
482 in rainfall variability over tropical oceans. It also prevented the inhibition of shallow
483 convection by deep convection, and that of deep convection by downdrafts and cold
484 pools. This concept of splitting the atmospheric column in different subcolumns might
485 be extended, in the future, to the boundary layer turbulence scheme and large-scale
486 condensation scheme. It would allow the processes to affect temperature and humidity
487 differently in the cloudy and clear portions of the cells. Adjusting the reevaporation
488 rate was an essential part of the development of LMDZ6A. This rate is based on the
489 fraction of overlying clouds (see step 1 of section 2.7) but still affects the humidity of
490 the whole gridbox. This splitting technique would make it possible to reevaporate rain
491 only in the cloudy portion of the cell.

492 *2.10.3 Revisiting basic thermodynamics*

493 The development of LMDZ6A also revealed the importance of a consistent ther-
494 modynamics by the implementation of the heat exchange due to the liquid \leftrightarrow ice
495 phase change and resulting changes in the entire cloud distribution. A disadvantage
496 of a multi-object framework is the difficulty in ensuring thermodynamical consistency
497 and energy conservation in the three different schemes.

498 *2.10.4 Tuning as a tool for identifying model weaknesses*

499 Finally, one essential lesson learned during the development of version 6A is the
500 need to tune the free parameters of the cloud schemes using well identified radiative
501 targets. Beyond the technical need to tune climate models, tuning helps improve the
502 physical formulations and identify model deficiencies “if parameter values needed to
503 satisfy a given metric are outside the acceptable range, or if different values are needed
504 for different regions or climate regimes” (Hourdin et al., 2017). We will later see, for
505 example, that the tuning of version 6A revealed a probable deficiency in the computa-
506 tion of high-level cloud cover and associated overlap assumptions (see section 5). The
507 tuning process is also a good way to reveal compensating errors.

508 **3 Model setup and evaluation**

509 The impact of the physics improvements described in section 2 on the cloud
510 structure and properties is analyzed using two 20-year AMIP-typed simulations that
511 are described in Table 2. We focus on the differences between versions 5A and 6A of
512 LMDZ, or more specifically between the atmospheric components of the IPSL-CM5A-
513 MR and IPSL-CM6A-LR models, which share the same horizontal grid (144 \times 142).
514 However, we don’t compare the two versions on the same vertical grid because the
515 vertical resolution is strongly tied to the physical parameterizations of each version
516 (39 levels for version 5A and 79 levels for version 6A). Thanks to the backward com-
517 patibility of LMDZ (Hourdin et al., 2020), the two simulations are run using the same
518 source code, but the simulation is configured with LMDZ5A parameterizations in one
519 case, and LMDZ6A parameterizations in the other. Version 5B is not analyzed in this
520 paper because it was in many respects a prototype of version 6A, as mentioned in the
521 introduction. The same aerosol concentration is used in both simulations, and is the

522 one used for the CMIP6 project (Lurton et al., 2020). Both simulations are run using
 523 the most recent version of the ORCHIDEE soil and vegetation scheme. This scheme
 524 computes the vertical water transport in the soil using the Richard’s equation (de
 525 Rosnay et al., 2002; d’Orgeval et al., 2008) discretized with 11 layers (see Cheruy et
 526 al., 2020, for more detail on the scheme and its impact on the results of IPSL-CM6A).

	LMDZ5A	LMDZ6A
Horizontal resolution	144×142	144×142
Vertical resolution	39 levels	79 levels
Run duration	20 years	20 years
Physics time step	30 min	15 min
Boundary and initial conditions	AMIP*	AMIP*
Coupling with soil model	ORCHIDEE	ORCHIDEE
	11 layers	11 layers

* Uses observed sea surface temperatures and sea ice concentration as lower boundary condition.

Table 2. Model configurations used in the present study.

527 The two simulations are tuned, meaning that some cloud parameters are adjusted
 528 (Hourdin et al., 2017). The tuning of LMDZ5A is described in section 3.4 of Hourdin,
 529 Grandpeix, et al. (2013), and the tuning of LMDZ6A is presented in Hourdin et al.
 530 (2020). When comparing the two simulations of the present paper, it is therefore im-
 531 portant to keep in mind that the two simulations are tuned by targeting in particular
 532 a good TOA (Top Of Atmosphere) global net flux. Some terms introduced in section 2
 533 differ between LMDZ5A and LMDZ6A: ξ_{300} in Figure 2, β in equation 12, τ_{conv} and
 534 q_{clw} in equation 14, γ_{iw} in equation 15 and r_{min} (the smallest ice particle size) in sec-
 535 tion 2.8. The maximum precipitation efficiency for deep convection ep_{max} is the same
 536 in the two simulations. The different values used for these parameters are summarized
 537 in Table 3. The role of each parameter in the tuning process is described in detail in
 538 Hourdin, Grandpeix, et al. (2013) and can be summarized as follows. Increasing β ,
 539 τ_{conv} or q_{clw} tends to increase the amount of low-level clouds but impacts differently
 540 on their vertical profile. Increasing r_{min} decreases the emissivity of high-level clouds.
 541 Increasing the γ_{iw} coefficient increases the conversion to precipitation in ice clouds and

542 decreases their water content. Increasing ep_{max} decreases the amount of detrained wa-
 543 ter and high-level clouds in convective regions. As mentioned in section 2.7, the ξ_{300}
 544 parameter has a strong impact on the relative humidity in the tropical upper tropo-
 545 sphere and controls the variance of the lognormal PDF used in the cloud statistical
 546 scheme of high-level clouds. The latter three parameters (γ_{iw} , ep_{max} and ξ_{300}) all
 547 affect the relative humidity of the tropical upper troposphere as they impact on the
 548 sources (ep_{max}) and sinks (γ_{iw} and ξ_{300}) of water vapor.

549 Since the two simulations are tuned, both simulations correspond to the same
 550 mean climate state. Therefore, differences between the two simulations mainly arise
 551 from changes in the model parameterizations, and to a lesser extent from slight changes
 552 in the values of the tuning parameters themselves. The impact of the physics timestep
 553 and the vertical resolution were also assessed using sensitivity experiments. Changing
 554 the physics timestep from 30 min to 15 min in version 5A has almost no impact on the
 555 results. The vertical resolution, however, has a noticeable impact on the results (as
 556 also noticed in other models, e.g. Xie et al., 2018), and changing the number of vertical
 557 levels from 39 to 79 levels in version 6A increases the trade-wind cumulus cloud cover
 558 by around 20% and the mid-level cloud cover in the ITCZ by around 60%.

Tuning parameter	LMDZ5A	LMDZ6A
ξ_{300}	(see Fig. 2)	(see Fig. 2)
β ($(\text{kg m}^{-2} \text{ s}^{-1})^{-1/2} \text{m}^{-1}$, see eq. 12)	2×10^{-5}	1×10^{-4}
τ_{conv} (seconds, see eq. 14)	1800	900
q_{clw} (g kg^{-1} , see eq. 14)	0.416	0.65
γ_{iw} (see eq. 15)	0.5	0.8
r_{min} (μm , see section 2.8)	3.5	16
ep_{max} (see section 2.3)	0.999	0.999

Table 3. Tuning parameters used in the two model configurations outlined in Table 2.

4 Results

4.1 Cloud spatial distribution

We first compare the simulated cloud distribution to the lidar-based GOCCP dataset (GCM Oriented CALIPSO Cloud Product, Chepfer et al., 2010). To do so, the cloud water contents and fractions predicted by LMDZ are processed by the CALIPSO-COSP simulator (Bodas-Salcedo et al., 2011) to derive the cloud fractions and covers the instrument would see if it was observing the model. To do so, the simulator uses the same overlap assumption as the LMDZ radiative transfer. *Note that in the present paper, the term “cloud fraction” refers to the 3D cloud fraction at each level and in each gridbox, whereas the term “cloud cover” refers to the total cloud cover seen from above, computed by integrating the 3D cloud fractions vertically assuming a given overlap of clouds within the vertical column of the model gridboxes.* This integral can be over the entire column or over a given pressure interval. In our case, we use three cloud covers that correspond to three cloud categories: low-level clouds (below 680 hPa or ~ 3 km), mid-level clouds (between 680 and 440 hPa, i.e. 3 km and 6.5 km) and high-level clouds (above 440 hPa or ~ 6.5 km). Figure 4 shows the cloud cover maps and bias maps of the three cloud categories whereas Fig. 5 shows the 3D cloud fractions. Table 4 also summarizes the mean bias between the model and the observations, the RMSE and the correlation coefficient.

Starting with low-level clouds, comparing Figures 4a, 4d, and 4g reveals a significant improvement in the low-level cloud covers over the tropical oceans in LMDZ6A. On the west side of ocean basins, trade-wind cumulus clouds were underestimated in version 5A, as can be seen in Figures 4a and 4g. In LMDZ6A, they reach a better agreement with the observations (see Figures 4a and 4d). On the east side of ocean basins, stratocumulus clouds are improved in LMDZ6A due to the new statistical cloud scheme and change in the detrainment formulation of the thermal plume model (see section 2.6). Low-level clouds were underestimated over the Indo-Pacific warm pool in LMDZ5A and are now better represented as well. As can be seen in the bias plots 4j and 4m, the overall bias is reduced in version 6A over the tropical oceans but stratocumulus cloud cover maxima are slightly shifted away from the coasts. As described in Hourdin et al. (2019), this shift might be due to the tendency of the LMDZ6A model to maintain a 100% cloud deck for too long during the transition from stratocumulus to

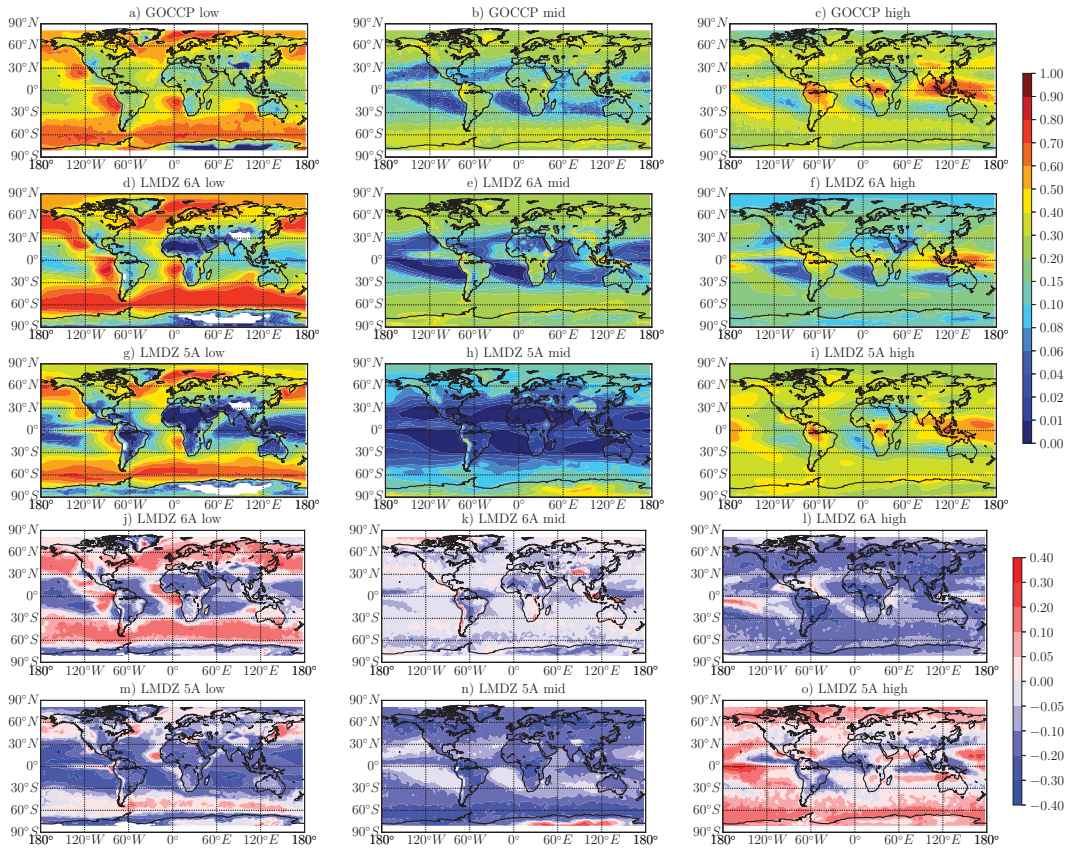


Figure 4. Panels a to i: Low, middle and high cloud cover from the CALIPSO-GOCCP climatology (averaged over the 2006–2009 period, top row) and from versions 6A and 5A of LMDZ (as computed by the CALIPSO-COSP simulator and averaged over a 20-year period). Panels j to o: Difference between the simulated cloud covers and the CALIPSO-GOCCP climatology. A positive value implies overestimation of the cloud cover by the model.

591 cumulus clouds. Outside the tropical belt, low-level clouds are overestimated over the
 592 Arctic and Southern Oceans. As evidenced in Figures 4j and 4m, this bias is stronger
 593 in version 6A than in version 5A. The overall RMSE for low-level clouds is reduced
 594 in version 6A (see Table 4), mostly thanks to the improvements seen in the tropical
 595 regions.

Cloud level Model version	Low-level		Mid-level		High-level	
	5A	6A	5A	6A	5A	6A
Mean bias	-0.106	-0.006	-0.144	-0.035	0.030	-0.122
RMSE	0.156	0.119	0.163	0.059	0.089	0.137
Correlation coefficient	0.829	0.840	0.543	0.741	0.628	0.758

Table 4. Mean bias, root-mean-square error and correlation coefficient for low, mid and high-level cloud covers between both versions of the model and the CALIPSO-GOCCP climatology. See Fig. 4 for context.

596 The mid-level cloud distribution is one of the most striking improvement of
 597 LMDZ6A. A comparison of Fig. 4b and 4e shows a reasonable agreement between the
 598 model and the observations, whereas previous versions of the model were systemati-
 599 cally underestimating mid-level clouds. This is due to the improvement of the deep and
 600 shallow convection schemes in the tropical and mid-latitude regions (see sections 2.3
 601 and 2.6), and to the new phase-partitioning of clouds in the mid- to high-latitude re-
 602 gions (see Fig. 3). As mentioned in section 3, the increase in vertical resolution from
 603 39 levels in version 5A to 79 levels in version 6A also improved mid-level cloud covers
 604 in the ITCZ. High-level clouds are however underestimated in LMDZ6A, which was
 605 not the case before (Fig. 4, right column). We had to reach a compromise in the tuning
 606 of the fall velocity parameter γ_{iw} , which is relatively high in version 6A (see Table 3).
 607 This tends to reduce the amount of high-level clouds globally to meet the LW CRE
 608 tuning target.

609 Figure 5 shows the zonal mean cloud fractions averaged over 20 years of sim-
 610 ulation in the two versions of the model and in the CALIPSO-GOCCP dataset. As
 611 already noticed in Fig. 4, outside the tropical belt, low-level clouds are overestimated
 612 in both LMDZ5A and 6A, but their altitude and fraction are improved in LMDZ6A.
 613 Their altitude of around 2 km is now slightly too high compared to the observations

614 where low-level clouds are mostly below 1.5 km. Interestingly, comparing Figure 5e
615 and 5h reveals that in version 6A, we actually decreased the 3D cloud fraction, but
616 increased the geometrical thickness of low-level clouds, thereby increasing the low-
617 level cloud cover (see Fig. 4d). Mid-level clouds were mostly absent in LMDZ5A and
618 are now better represented (see Fig. 5e and 5h), especially over mid- to high-latitude
619 regions. This is also evidenced by the mean bias, RMSE and correlation coefficient
620 shown in Table 4. In the tropics, LMDZ6A shows a local maximum in mid-level cloud
621 cover slightly below 5 km altitude. The same maximum is located more than a 1000 m
622 higher in the observations, at elevations devoid of any cloud in the model. Another
623 striking improvement of version 6A is the water phase-partitioning in mid- to high-
624 level clouds. In LMDZ5A, the ice-phase cloud fraction was clearly overestimated (see
625 Fig. 5i) and not consistent with the observations (Cesana et al., 2015). Changing the
626 phase-partitioning in mixed-phase clouds (as shown in Fig. 3) significantly improved
627 the ice-phase cloud fractions in LMDZ6A (Fig. 5, right column), as well as the liquid-
628 phase cloud fractions in mid-level clouds (middle column). As previously mentioned,
629 high-level cloud cover remains underestimated due to a compromise in the tuning of
630 the model, but their spatial distribution is improved (see Fig.4f and correlation coef-
631 ficients in Table 4). High-level 3D cloud fractions are overestimated in the tropical
632 regions if we compare Figures 5c and 5f, but their total column cloud cover is under-
633 estimated in this same region if we look at Fig. 4f and upper-left panel of Fig. 8. This
634 suggests, as will be discussed in section 5, that the cloud cover computed by the model
635 for high-level clouds is too low and compensated by a too high 3D cloud fraction.

636 Figure 6 focuses on the cloud fraction in the tropical regions, more exactly on the
637 GPCI transect, which spans from San-Francisco to Honolulu (see Teixeira et al., 2011,
638 for more detail). This transect is especially useful to evaluate the representation of
639 the stratocumulus to cumulus (Sc-to-Cu) and shallow to deep convection transitions in
640 climate models. In LMDZ5A, the Sc-to-Cu transition was visible, but stratocumulus
641 clouds were too close to the surface and high-level cloud fractions were overestimated.
642 Version 6A nicely represents the Sc-to-Cu transition and shows a better evolution of
643 the cloudy boundary layer, but clouds tend to extend beyond the 2 km height seen in
644 the observations. Over the warmer waters of the trade-wind boundary layer (around
645 5°N), the model cloud fractions remain too low compared to the observations. Mid-
646 level cloud fractions are also underestimated in deep convective regimes, as is also

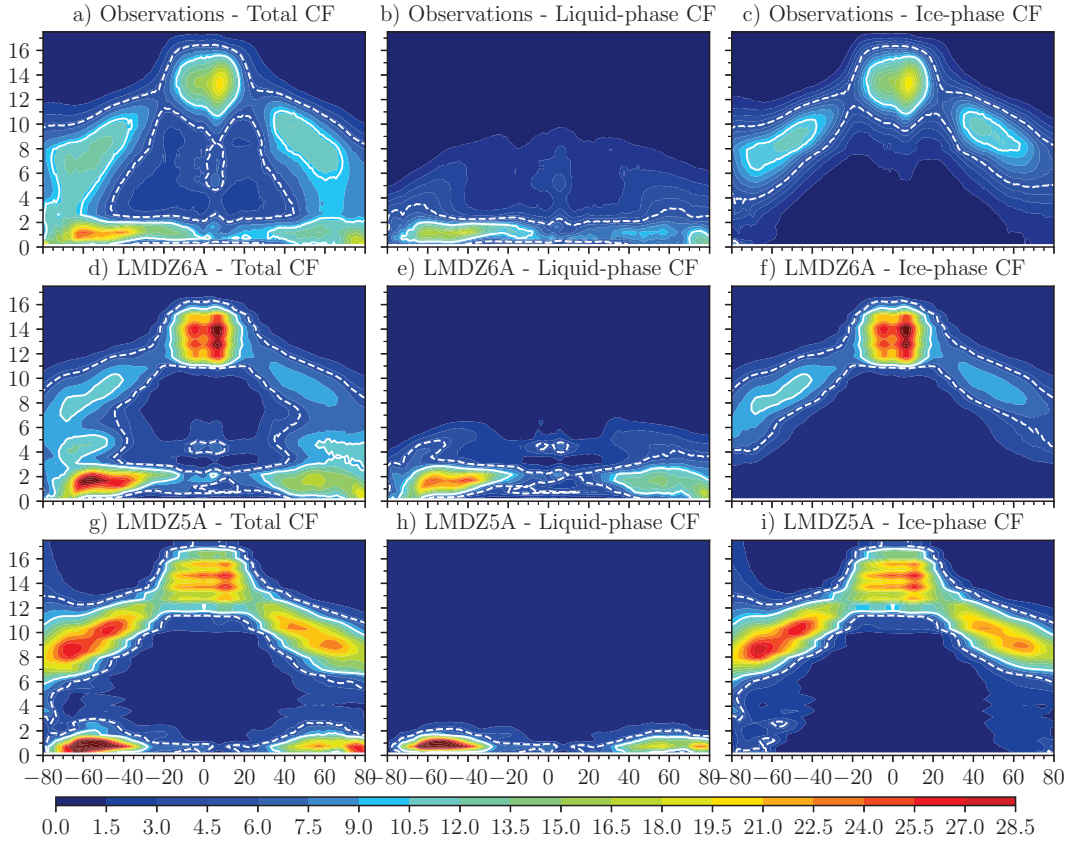


Figure 5. Zonally-averaged vertical structure of the cloud fractions predicted by LMDZ5A and 6A (20 year average) using the COSP simulator (middle and bottom rows) compared against the CALIPSO-GOCCP climatology (top row). Y-axis gives the altitude above the local surface in km. The dotted and solid white contours represent the 0.05 and 0.1 cloud fractions, respectively. The left column gives the total cloud fraction, the middle column the liquid-phase cloud fraction, and the right column the ice-phase cloud fraction.

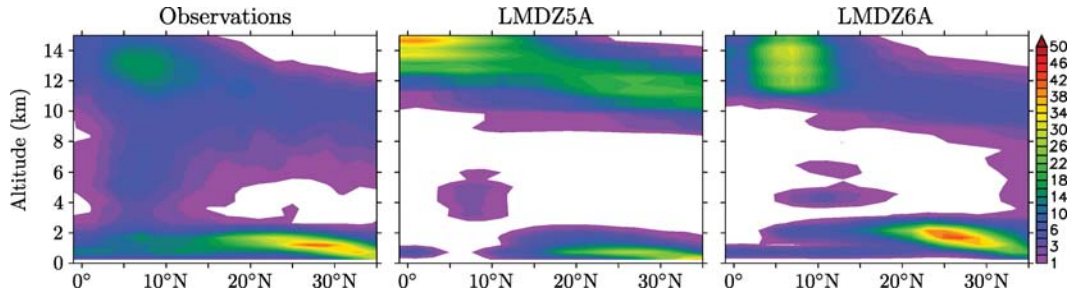


Figure 6. Cross-section of the cloud fraction along the GPCI transect (GCSS/WGNE Pacific Cross-Section Intercomparison, Teixeira et al., 2011) as observed by CALIPSO-GOCCP over the 2006–2009 period (left panel) and simulated by LMDZ5A (middle panel) and LMDZ6A (right panel) over a 20-year period.

647 noticed in Fig. 5d at around 8 km altitude. This altitude range is where the $\xi(p)$
 648 function sharply increases (see Fig. 2). It is therefore in the transition zone between
 649 the PDFs of the shallow convection, deep convection and large-scale condensation
 650 schemes, and suggests that the interplay between the schemes need to be improved in
 651 this region. The high-level cloud fraction is better represented in LMDZ6A but clouds
 652 remain too geometrically thin compared to the observations.

653 4.2 Cloud radiative effect (CRE)

654 Clouds play a crucial role in the radiative budget of the atmosphere, and a
 655 compromise has often to be found between a good representation of their properties
 656 and a good TOA energy budget of the model. The tuning method of LMDZ6A is
 657 described in Hourdin et al. (2020), and we focus here on the role of clouds in the
 658 radiative budget.

659 Figure 7 shows the observed and simulated CRE in the SW and LW domains,
 660 as well as the bias maps. The left column of this figure shows a clear improvement
 661 of the SW CRE, especially in mid- to high-latitude regions where reflection by low-
 662 level clouds was too high in version 5A. This improvement results in a 5 W m^{-2}
 663 reduction of the SW CRE mean bias and RMSE in LMDZ6A, as shown in Table 5.
 664 An improvement of the same magnitude is seen in the LW CRE, but in this latter case,
 665 the spatial distribution is also improved (see the increase in the correlation coefficient
 666 in Table 5), which is less the case of the SW CRE, especially in the tropical regions.

667 Indeed, despite a clear improvement of the SW CRE in the ITCZ (see Fig. 7c), the SW
 668 radiative effect of stratocumulus clouds is shifted away from the coast over the eastern
 669 part of tropical ocean basins, and trade-wind cumulus clouds reflect less sunlight than
 670 in the observations (see Fig. 7g). These biases are consistent with those of the low-level
 671 cloud cover described in section 4.1.

CRE wavelength range Model version	Shortwave		Longwave	
	5A	6A	5A	6A
Mean bias	-5.043	-0.795	5.932	-0.818
RMSE	14.916	9.150	9.224	4.630
Correlation coefficient	0.827	0.881	0.708	0.855

Table 5. Mean bias, root-mean-square error and correlation coefficient for SW and LW CRE between both versions of the model and the CERES observations (Loeb et al., 2009). See Fig. 7 for context.

672 The left column of Fig. 8 summarizes the zonal mean cloud cover of the three
 673 cloud categories and the corresponding radiative forcings in the right column. In the
 674 tropics, cloud covers are improved in LMDZ6A at all levels, but remain slightly lower
 675 than in the observations. The right column of Fig. 8 shows that in this region a
 676 realistic CRE is reached even though the cloud covers are slightly biased low. For
 677 high-level clouds, this suggests that the underestimated cloud covers are probably
 678 compensated by a too high 3D cloud fraction. For low-level clouds, it suggests that
 679 the underestimated cloud cover is compensated by overly bright low-level clouds, as
 680 will be discussed in section 5. The situation is different over the Arctic and Southern
 681 oceans, where a realistic CRE is reached even though the low-level cloud covers are
 682 biased high (see Fig. 7c, 7d and Fig. 8, lower left panel). In these regions, the LMDZ6A
 683 SW CRE is in better agreement with the observations than that of LMDZ5A, and this
 684 has to do with cloud phase and opacity, as we will see in the next paragraph. It is
 685 worth noting that this difference in low-level cloud covers between the two versions
 686 could have come from the results of the simulator because of the possible screening of
 687 low-level clouds by high-level clouds. In our case, high-level cloud covers are biased
 688 low relative to the observations in version 6A (see Fig. 4l) and could increase the signal
 689 coming from low-level clouds and partly explain the positive cloud cover bias seen in

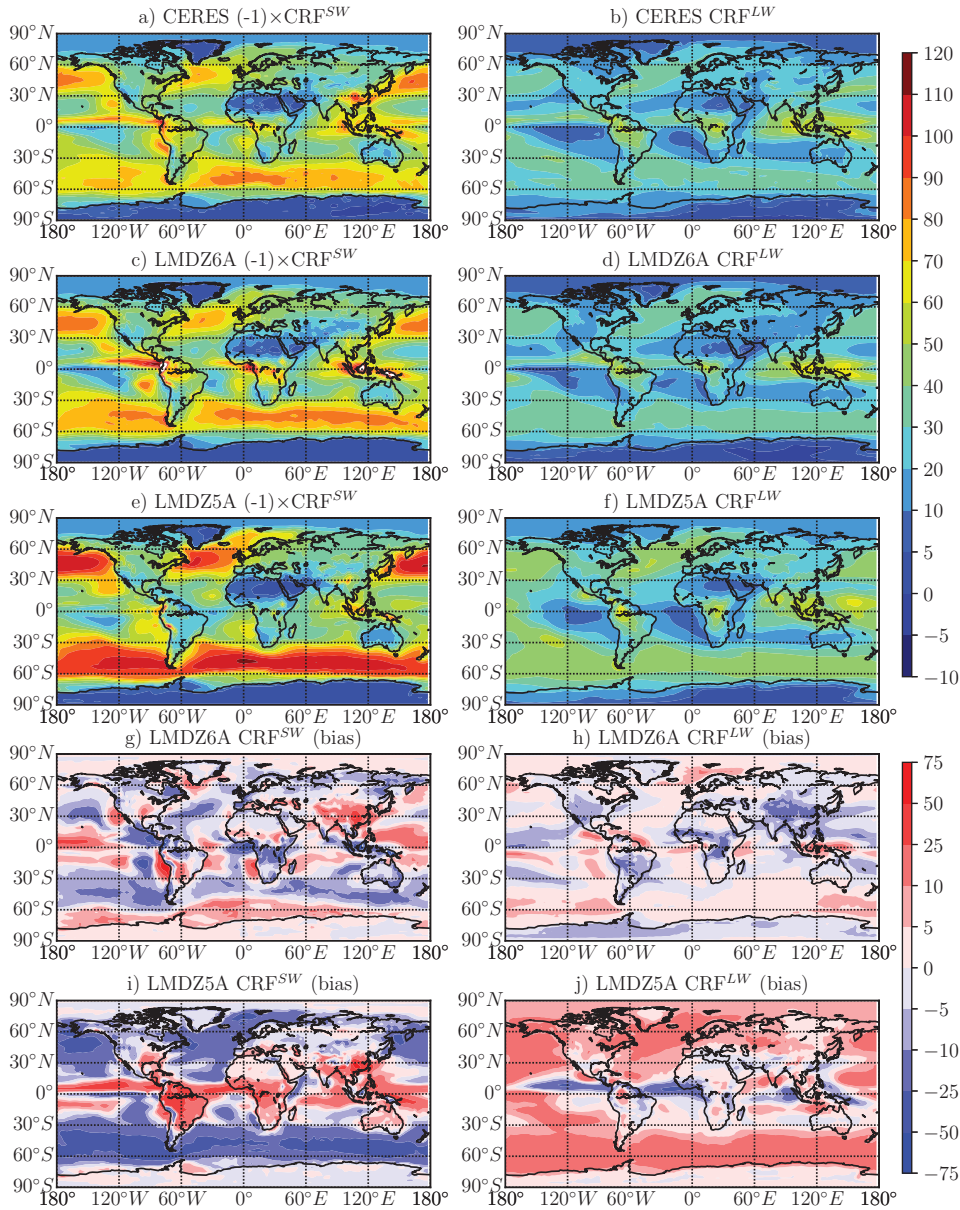


Figure 7. Panels a to f: Shortwave (left column) and longwave (right column) cloud radiative effect (CRE) in W m^{-2} observed by CERES (averaged over a 16-year period, Loeb et al., 2009) and simulated by version 6A (panels c and d) and version 5A (panels e and f) of the LMDZ climate model (averaged over a 20-year period). To make use of a common color scale, the opposite of the SW CRE is represented: a positive value thus corresponds to an increased reflection and decrease in the amount of solar radiation absorbed by the Earth relative to clear-sky conditions. Panels g to j: bias plots for version 6A (panels g and h) and version 5A (panels i and j). A positive value of the SW CRE bias implies overestimation of the SW CRE by the model (not enough reflection by clouds), and a positive value of the LW CRE bias implies overestimation of the LW CRE by the model (too much greenhouse effect of clouds).

690 Figure 4d. But this is not the case. We find the same difference between the low-level
 691 cloud covers of version 5A and 6A using the results of the model radiative transfer
 692 itself (not the simulator).

693 Let’s now return to the good total CRE simulated in LMDZ6A in mid- to high-
 694 latitude regions despite the biases seen in the various cloud covers (Fig. 8). In mid- to
 695 high-latitude regions, phase-partitioning has been found to be strongly connected to
 696 the SW CRE in many models (McCoy et al., 2016). In our case, sensitivity experiments
 697 show that increasing the temperature range of supercooled droplets leads to a greater
 698 vertical extension of liquid clouds, which are otherwise confined to lower layers. This
 699 results in a higher concentration, in LMDZ6A, of liquid droplets in mid-level clouds,
 700 where droplets are more reflective than ice (Liou, 2002), but more importantly in a
 701 lower concentration of droplets in low-level clouds. This decrease in the concentration
 702 of liquid droplets in low-level clouds explains why the SW CRE is in better agreement
 703 with the observations in LMDZ6A, despite the overestimation of the low-level cloud
 704 cover. The LW CRE is also sensitive to phase-partitioning in mixed phase clouds. The
 705 left column of Fig. 8 shows that LMDZ6A has less high-level clouds and more mid-level
 706 clouds in mid- to high- latitude regions. Decreasing the high-level cloud cover decreases
 707 the LW CRE, but on the other hand, the increase in mid-level cloud covers of high
 708 liquid content strongly increases it. In the end, the LW CRE in LMDZ6A is reduced
 709 by the right amount compared to that of LMDZ5A and is in good agreement with the
 710 observations. The overall cloud liquid water path in mid- to high-latitude regions is
 711 increased, as illustrated in Fig. 9, whereas the ice water path is strongly decreased.
 712 Satellite retrieval of the LWP and IWP is not an easy task, but a comparison of
 713 the simulated LWP with the work of O’Dell et al. (2008) suggests that it is in good
 714 agreement with the observations in the tropical regions and slightly too high in mid-
 715 to high-latitude regions. It is more difficult to compare the simulated cloud IWP (i.e.
 716 the non-precipitating ice) to existing observations, but the sharp decrease in the cloud
 717 IWP of version 6A is more in line with the cloud IWP found in other models, including
 718 the ERA5 and MERRA-2 reanalyses (see Fig. 3 of Duncan & Eriksson, 2018).

719 Figure 10 focuses on the tropics and shows the simulated cloud radiative effect
 720 as a function of the dynamical regimes (through the vertical velocity ω at 500 hPa).
 721 This type of analysis, introduced by Bony et al. (2004), shows how well the CRE is
 722 represented in regions of subsidence ($\omega > 0$) and updraft ($\omega < 0$). Both the SW and

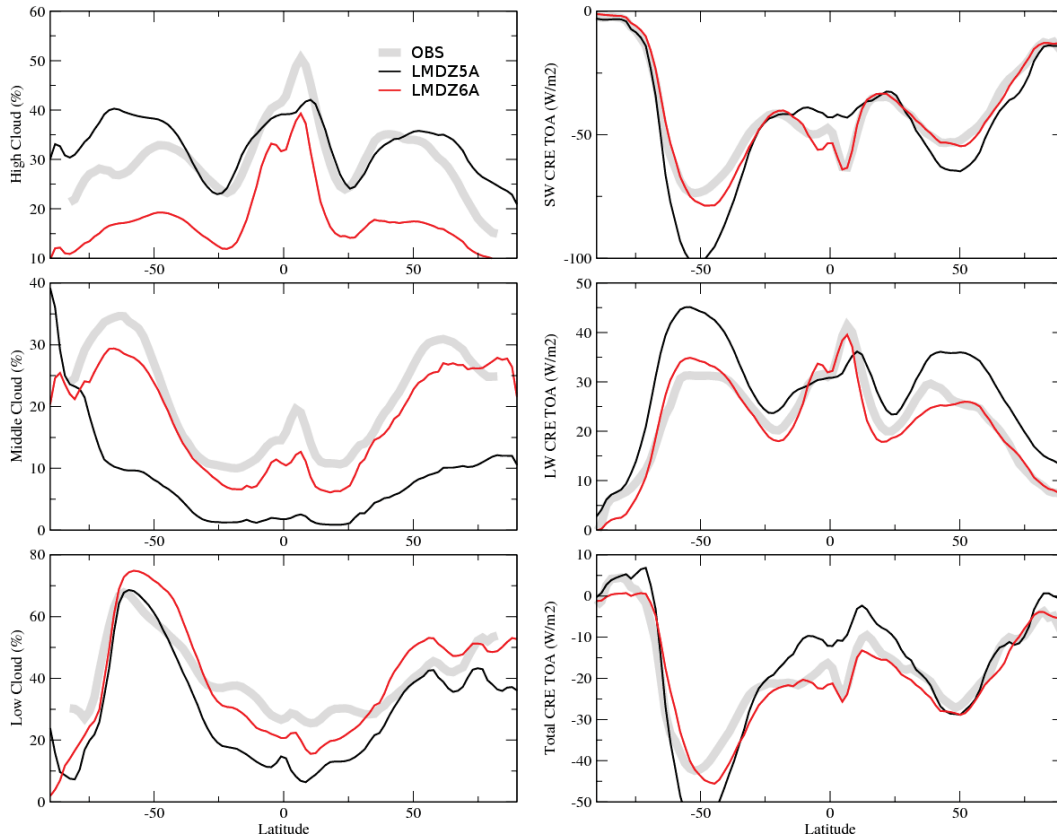


Figure 8. *Left column:* Zonal mean cloud covers simulated by LMDZ5A and 6A (20 year average) using the COSP simulator, compared against the CALIPSO-GOCCP climatology (in gray). *Right column:* Zonal mean TOA (Top Of Atmosphere) SW (top panel), LW (middle panel) and total (lower panel) CRE (Cloud Radiative Effect) predicted by LMDZ5A and 6A (20 year average) and observed by the CERES instruments (EBAF dataset, Loeb et al., 2009).

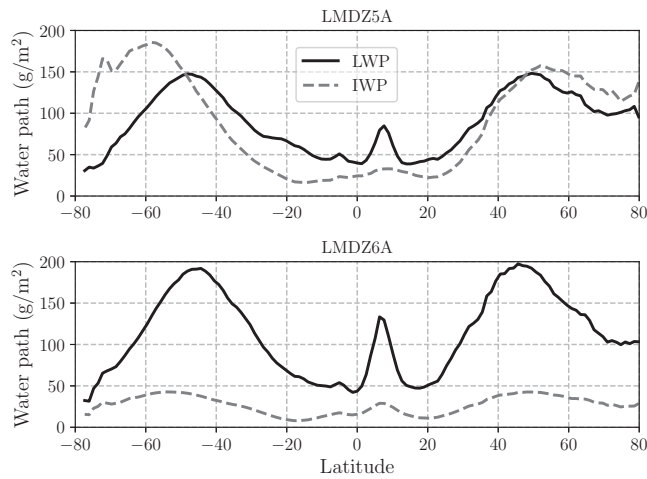


Figure 9. Cloud LWP and IWP (liquid and ice water paths in g m^{-2}) over oceans in LMDZ5A (top) and LMDZ6A (bottom).

723 LW CREs show a gradual decrease (in terms of absolute value for the SW CRE) from
 724 regions of strong updrafts where clouds are abundant to regions of strong subsidence
 725 where clouds dissipate. The lower panel of Fig. 10 shows a clear improvement of
 726 the total CRE in LMDZ6A in convective regions ($\omega < 0$). This is mostly due to
 727 an improvement of the SW CRE (upper panel), and reflects the changes applied to
 728 the thermal plume parameterization, which improved both the stratocumulus clouds
 729 over the eastern part of tropical ocean basins and trade-wind cumulus clouds (see
 730 section 4.1). However, the SW and LW CREs are still too weak in magnitude in
 731 strongly convective regions ($\omega < -40$ hPa/day) and the SW CRE is higher than
 732 observed in regions of strong subsidence ($\omega > 20$ hPa/day).

733 5 Discussion

734 Thanks to the improvements of the physical parameterizations and to an experi-
 735 ence gained in the tuning of the model, the cloud distribution and radiative effects
 736 have been significantly improved in LMDZ6A. But the refined tuning of the model has
 737 also underlined structural problems, especially in the detailed cloud radiative proper-
 738 ties. In particular, the difficulty to tune high-level clouds points to an inappropriate
 739 representation of their radiative properties, which impacts on all clouds. Difficulties in
 740 modeling the properties of high-level clouds were already found in the early versions of
 741 LMDZ (Webb et al., 2001). Figure 11 shows the PDF of the high-level cloud cover over
 742 the tropical oceans based on the daily outputs of the CALIPSO-GOCCP observations
 743 (left panel) and results of the LMDZ model simulator (middle and right panels). The
 744 observed PDF is a highly skewed-right distribution with a peak at 0–5% cloud cover
 745 and an outlier at 97.5–100%. The LMDZ5A PDF shows a lower peak at 0–5% but an
 746 otherwise similar distribution, with a smaller outlier at 97.5–100%. LMDZ6A shows a
 747 skewed-right distribution similar to the observations for cloud cover lower than 20%,
 748 but its PDF differs significantly for higher cloud covers, with a strong decrease above
 749 50% and no outlier at 97.5–100%. This difficulty of LMDZ6A to attain complete cov-
 750 erage for high-level clouds might explain why these clouds are hard to tune in this
 751 version. Therefore, work is underway to improve the ξ function (see section 2.7) using
 752 a more physical parameterization, as well as the overlap assumptions and subgrid scale
 753 heterogeneities of high-level clouds.

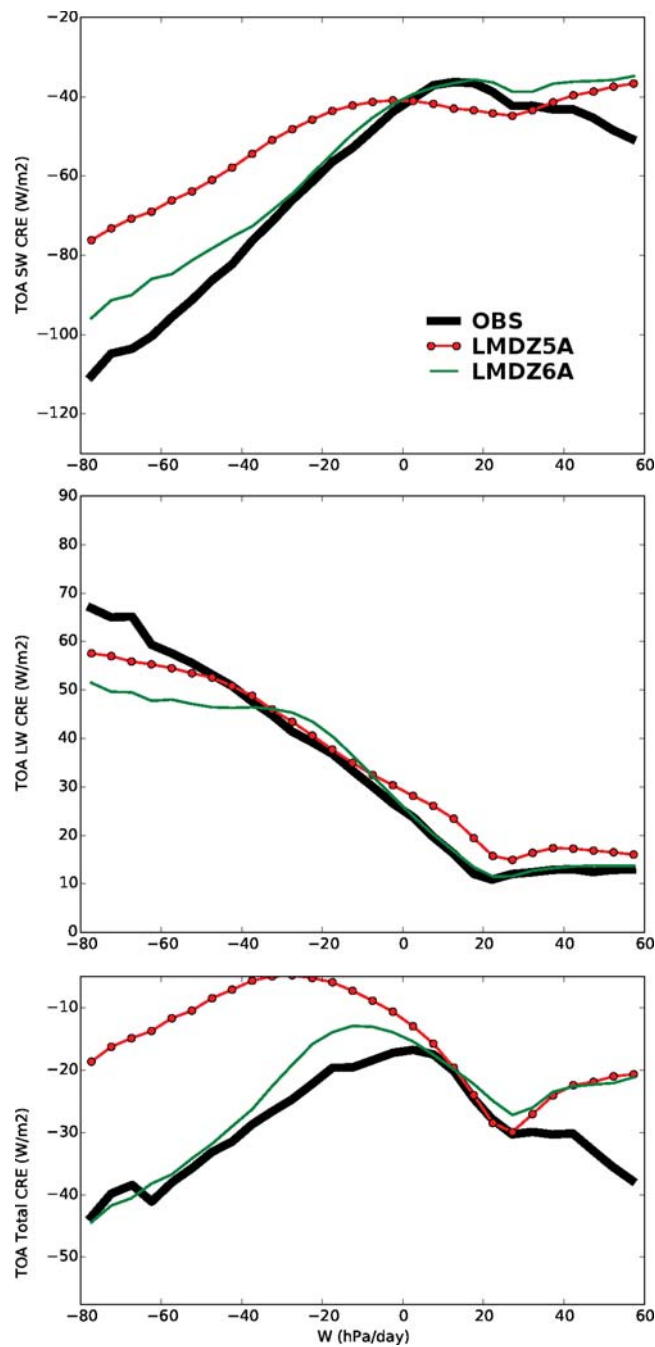


Figure 10. Regime sorted plots of the SW (upper row), LW (middle row) and net (lower row) CRE as a function of ω_{500} in hPa/day between 30°S and 30°N and over the oceans. For comparison, the black line shows the same diagnostics obtained using ERA reanalysis and the CERES data (EBAF dataset, Loeb et al., 2009).

754 Regarding tropical low-level clouds, Figure 12 shows the density of points of
755 a given cloud reflectance and cloud cover in the observations (left panel) and in the
756 model (middle and right panels, see Konsta et al., 2016, for more detail on the method).
757 Cloud reflectance in Fig. 12 is a function of the vertically integrated cloud optical depth,
758 whereas cloud cover will be more dependent on the cloud fraction vertical profiles and
759 overlap assumption. Two populations can be identified in the observations (Fig. 12,
760 left panel): trade-wind cumulus clouds have low reflectance and cover values, whereas
761 stratocumulus clouds have medium reflectance and high cover values. The observations
762 also show an increase in cloud reflectance with increasing cloud cover. LMDZ5A was
763 showing the opposite tendency (Fig. 12, middle panel) and trade-wind cumulus clouds
764 were too bright in this version of the model, a problem commonly referred to as the
765 “too few, too bright” problem (Nam et al., 2012). As explained in Konsta et al. (2016),
766 this increase in reflectance with decreasing cloud fraction in LMDZ5A was due to the
767 activation of the deep convection scheme in trade-wind regions, which affected the
768 low-level cloud PDFs. The implementation of the thermal plume model in LMDZ6A
769 clearly improved the distribution, which is now closer to the observations (Fig. 12, right
770 panel). However, in LMDZ6A, trade-wind cumulus clouds are still too reflective and
771 their cover is too low. Stratocumulus clouds are well represented and show medium
772 reflectance and high cover values, in agreement with the observations. Between these
773 two populations, a third population appears in the model, and is characterized by
774 cloud reflectance values of around 0.2 and cover values between 0.6 and 0.9. The too
775 few, too bright bias was thus reduced but not fully solved. Despite the high number in
776 LMDZ6A of low cloud cover values compared to the observations (Fig. 12, right panel),
777 the SW CRE is still in good agreement with the observations. This suggests that this
778 too low cover is compensated by an excessive brightness in the tuning process, which
779 targets the cloud radiative effect as a priority. We thus see cloud reflectances of around
780 0.3 in LMDZ6A, compared to less than 0.1 in the observations (see Fig. 12, left and
781 right panels). This shows the limit of the maximum-random overlap assumption used
782 in LMDZ6A. Preliminary sensitivity experiments performed with LMDZ6A shows that
783 using the exponential-random overlap assumption (Hogan & Illingworth, 2000) instead
784 of the maximum-random overlap assumption may improve the distribution shown in
785 Fig. 12 by increasing cumulus cloud cover. Another way to increase low-level cloud
786 covers is to represent subgrid scale vertical heterogeneities by distinguishing the cloud

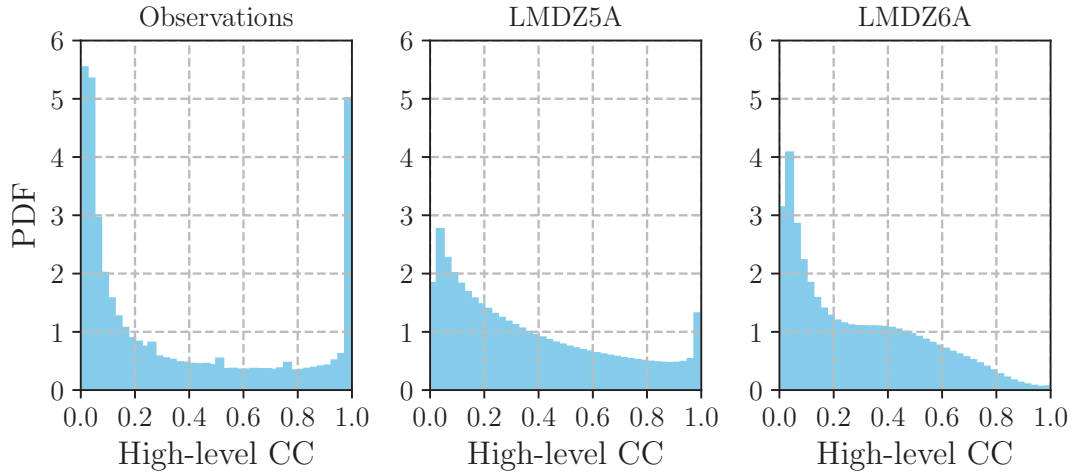


Figure 11. PDF of the high-level cloud cover over the tropical oceans. Left panel: CALIPSO-GOCCP daily observations over the 2007–2008 period. Middle and right panels: daily cloud covers computed by the CALIPSO-COSP simulator in versions 5A and 6A of LMDZ over a 10-year period.

787 fraction by volume from the cloud fraction by surface. The latter was found to be 20%
 788 greater on average than the cloud fraction by volume (Brooks et al., 2005). The cloud
 789 fraction by surface is more appropriate for coupling with radiative transfer schemes but
 790 most climate models do not yet distinguish between the two quantities and by doing
 791 so, assume that the cloudy area of a gridbox fills the entire gridbox in the vertical. The
 792 difference between the cloud fraction by volume and the cloud fraction by surface can
 793 be computed by a parameterization of subgrid scale heterogeneities that will depend
 794 on the vertical resolution and various physical information, such as wind shear for
 795 example (Sulak et al., 2020). Work is underway to implement such parameterization
 796 in LMDZ (Jouhaud et al., 2018). This could improve the CRE of low-level clouds but
 797 also high-level clouds.

798 **6 Conclusion**

799 After a series of parameterization changes (summarized in section 2.9) and a finer
 800 tuning of the radiative budget, several cloud features were improved in version 6A of
 801 the LMDZ climate model :

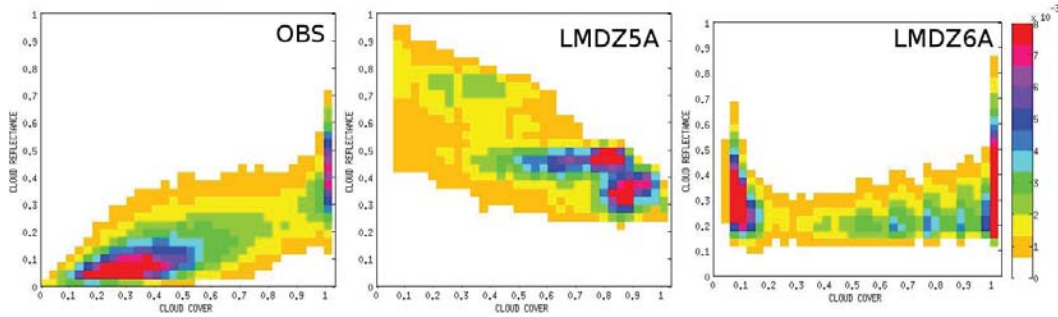


Figure 12. 2D histograms of low-level cloud reflectances and covers over the tropical oceans (30°S–30°N) observed by PARASOL and CALIPSO-GOCCP (left panel) and simulated by LMDZ5A (middle panel) and LMDZ6A (right panel) using instantaneous outputs (Konsta et al., 2016).

- 802 • Low-level (below 3 km) cloud covers are improved both in trade-wind regions and
- 803 in the east side of ocean basins (see Fig. 4d), due to the new shallow convection
- 804 scheme;
- 805 • Mid-level clouds, which were almost inexistent in LMDZ5A, are much better
- 806 represented in LMDZ6A (see Fig. 4e). Mid- to high-level cloud phase is also
- 807 more realistic and now includes a more realistic fraction of supercooled liquid
- 808 droplets (see Fig. 5e). These improvements mostly come from the changes made
- 809 in the deep convection scheme in the tropical regions, and in the new phase-
- 810 partitioning in the mid- to high-latitude regions;
- 811 • Cloud radiative effects are improved (see Fig. 8, right column) and LMDZ6A
- 812 shows a 5 W m^{-2} improvement in both the SW and LW CRE compared to
- 813 LMDZ5A (see table 5), due to the combined effect of the new shallow convection
- 814 scheme and new phase-partitioning;
- 815 • A 20 W m^{-2} bias in the SW cloud radiative effect of the convective regions is
- 816 corrected (see Fig. 10, upper panel), thanks mostly to the new shallow convection
- 817 scheme;
- 818 • Tropical low-level cloud reflectance and cover are significantly improved (see
- 819 Fig. 12, right panel) due to the shallow convection scheme and its new statistical
- 820 cloud scheme based on a Bi-gaussian PDF.

821 The finer model tuning performed for LMDZ6A also revealed structural errors
822 and inconsistencies that call for a revisit of some existing parameterizations. Indeed,
823 the model reaches a good radiative balance for cloud covers that are sometimes strongly
824 biased. This is true for low-level clouds but more importantly for high-level clouds,
825 whose covers need to be lower than observed to restore the radiative balance. For
826 clouds of all levels, work is underway to improve the overlap assumptions of the radia-
827 tive transfer scheme and to better account for the cloud subgrid scale heterogeneities
828 (see for example Jouhaud et al., 2018). High-level clouds also rely on a fixed value
829 of the lognormal PDF variance (ξ_{300}) which must be improved and more physically
830 based. Mid-level clouds are also the focus of current development efforts, in order to
831 better represent the deepening of shallow cumulus clouds into congestus clouds (see
832 Fig. 6). Improvement of the cloud microphysical scheme is also underway, with a par-
833 ticular focus on cold and mixed-phase clouds. Priorities include the improvement of
834 the conversion of ice clouds to solid precipitation (Lemonnier et al., 2020), the im-
835 plementation of supersaturation with respect to ice (Genthon et al., 2017), and the
836 representation of subgrid scale processes in mixed phase clouds.

837

Appendix A Notations

ρ	Atmospheric density	kg m^{-3}
ω_{500}	Large-scale vertical velocity at 500 hPa	hPa day^{-1}
θ	Potential temperature	K
q_v	Water vapor mass mixing ratio	kg kg^{-1}
q_l	Liquid water mass mixing ratio	kg kg^{-1}
q_i	Ice mass mixing ratio	kg kg^{-1}
q_t	Total water mass mixing ratio	kg kg^{-1}
q_{t_c}	Gridbox mean amount of condensate and in-cloud vapor	kg kg^{-1}
q_{sat}	Saturation mass mixing ratio	kg kg^{-1}
s	Saturation deficit (see Eq. 3 of Jam et al., 2013)	kg kg^{-1}
$P(q)$	Probability Density Function (PDF) of water vapor q	–
$Q(s)$	Probability Density Function (PDF) of the saturation deficit s	–
ALE	Available Lifting Energy	J kg^{-1}
ALP	Available Lifting Power	W m^{-2}
w_{iw}	Fall velocity of ice crystals	m s^{-1}
w_0	Terminal fall velocity of ice crystals	m s^{-1}
$P_{l,i}$	Liquid/Ice precipitation flux density	$\text{kg m}^{-2} \text{s}^{-1}$
$d\theta_{dw}^{cv}$	Temperature tendency due to downdrafts	K s^{-1}
$dq_{t,dw}^{cv}$	Total water tendency due to downdrafts	$\text{kg kg}^{-1} \text{s}^{-1}$
α_{th}	Coverage fraction of thermals	–
θ_{env}	θ in the environment of the plume	K
$q_{t,env}$	Mean q_t in the environment of the plumes	kg kg^{-1}
s_{env}	Saturation deficit in the environment of the plumes	kg kg^{-1}
σ_{env}	σ of the PDF related to the environment of the plumes	kg kg^{-1}
s_{th}	Saturation deficit inside the plumes	kg kg^{-1}
σ_{th}	σ of the PDF related to the plumes	kg kg^{-1}
q_c^{in}	In-cloud water mass mixing ratio	kg kg^{-1}
α_c	Cloud fraction	–

838

q_m	Condensed water mixing ratio in the mixed drafts	kg kg^{-1}
M_t	Mass flux density of the mixed drafts	$\text{kg m}^{-2} \text{s}^{-1}$
α_m	Coverage fraction of mixed drafts	–
τ_m	Dissipation time constant of the saturated drafts	s
δz	Vertical spacing of gridboxes	m
M_a	Mass flux density of the undiluted updrafts	$\text{kg m}^{-2} \text{s}^{-1}$
α_a	Coverage fraction of undiluted updrafts	–
w_a	Vertical velocity of the undiluted updrafts	m s^{-1}

When written in superscript, *th*, *wk*, *cv* and *lsc* indicates variables related to thermal plumes, wakes, deep convection and large-scale condensation, respectively.

For a list of the tuning parameters and their notations, see Table 3.

Acknowledgments

The last version of the LMDZ source code can be downloaded freely from the LMDZ web site. The version used for the specific simulation runs of this paper is the `svn` release 3404 from 2018/10/16 which can be downloaded and installed on a Linux computer by running the `install_lmdz.sh` script available online on the LMDZ website. A large part of the outputs is archived on the CMIP5 and CMIP6 archives, distributed through the Earth System Grid Federation (ESGF) and freely accessible through the ESGF data portals after registration. Lighter, pre-processed files will be made available with a DOI if the paper is accepted for publication, together with the scripts used to generate the figures. JBM thanks Christophe Genthon, Laurent Li, Jean Jouhaud for useful scientific discussions, Julie Celton-Madeleine for proofreading the manuscript, and Jérôme Servonnat and Karine Marquois for technical assistance. This study benefited from the IPSL mesocenter ESPRI facility which is supported by CNRS, Sorbonne University, Labex LIPSL, CNES, and Ecole Polytechnique. It was supported by CNRS and by CNES and granted access to the HPC resources of IDRIS under allocation 0292 made by GENCI. It was also supported by the DEPHY2 project funded by the French national program LEFE/INSU. We finally thank the JAMES editorial team and two anonymous referees for their thoughtful comments, which very much improved the quality of the manuscript.

References

- 862
- 863 Betts, A. K. (1973). Non-precipitating cumulus convection and its parameterization.
 864 *Quarterly Journal of the Royal Meteorological Society*, *99*(419), 178–196. doi:
 865 10.1002/qj.49709941915
- 866 Bodas-Salcedo, A., Webb, M. J., Bony, S., Chepfer, H., Dufresne, J. L., Klein, S. A.,
 867 ... John, V. O. (2011, Aug). COSP: Satellite simulation software for model
 868 assessment. *Bulletin of the American Meteorological Society*, *92*(8), 1023-1043.
 869 doi: 10.1175/2011BAMS2856.1
- 870 Bony, S., Colman, R., Kattsov, V. M., Allan, R. P., Bretherton, C. S., Dufresne,
 871 J.-L., ... Webb, M. J. (2006). How Well Do We Understand and Evaluate
 872 Climate Change Feedback Processes? *Journal of Climate*, *19*, 3445. doi:
 873 10.1175/JCLI3819.1
- 874 Bony, S., Dufresne, J.-L., Le Treut, H., Morcrette, J.-J., & Senior, C. (2004). On dy-
 875 namic and thermodynamic components of cloud changes. *Climate Dynamics*,
 876 *22*, 71-86. doi: 10.1007/s00382-003-0369-6
- 877 Bony, S., & Emanuel, K. A. (2001, November). A Parameterization of the
 878 Cloudiness Associated with Cumulus Convection; Evaluation Using TOGA
 879 COARE Data. *Journal of Atmospheric Sciences*, *58*, 3158-3183. doi:
 880 10.1175/1520-0469(2001)058<3158:APOTCA>2.0.CO;2
- 881 Boucher, O., & Lohmann, U. (1995, July). The sulfate-CCN-cloud albedo effect.
 882 *Tellus Series B Chemical and Physical Meteorology B*, *47*, 281. doi: 10.1034/j
 883 .1600-0889.47.issue3.1.x
- 884 Boucher, O., Servonnat, J., Albright, A. L., Aumont, O., Balkanski, Y., Bastrikov,
 885 V., ... Vuichard, N. (2020). Presentation and evaluation of the IPSL-
 886 CM6A-LR climate model. *Journal of Advances in Modeling Earth Systems*,
 887 e2019MS002010. doi: 10.1029/2019MS002010
- 888 Brooks, M. E., Hogan, R. J., & Illingworth, A. J. (2005, July). Parameterizing
 889 the Difference in Cloud Fraction Defined by Area and by Volume as Observed
 890 with Radar and Lidar. *Journal of Atmospheric Sciences*, *62*, 2248-2260. doi:
 891 10.1175/JAS3467.1
- 892 Cesana, G., & Chepfer, H. (2013, July). Evaluation of the cloud thermodynamic
 893 phase in a climate model using CALIPSO-GOCCP. *Journal of Geophysical Re-
 894 search (Atmospheres)*, *118*, 7922-7937. doi: 10.1002/jgrd.50376

- 895 Cesana, G., Waliser, D. E., Jiang, X., & Li, J. L. F. (2015, Aug). Multimodel
 896 evaluation of cloud phase transition using satellite and reanalysis data.
 897 *Journal of Geophysical Research (Atmospheres)*, *120*(15), 7871-7892. doi:
 898 10.1002/2014JD022932
- 899 Chepfer, H., Bony, S., Winker, D., Cesana, G., Dufresne, J. L., Minnis, P., ... Zeng,
 900 S. (2010, Jan). The GCM-Oriented CALIPSO Cloud Product (CALIPSO-
 901 GOCCP). *Journal of Geophysical Research (Atmospheres)*, *115*(D4), D00H16.
 902 doi: 10.1029/2009JD012251
- 903 Cheruy, F., Ducharne, A., Hourdin, F., Musat, I., Vignon, E., Gastineau, G., ...
 904 Yanfeng, Z. (2020). *Improved near surface continental climate in IPSL-
 905 CM6A-LR by combined evolutions of atmospheric and land surface physics.*
 906 (Submitted to JAMES) doi: 2019MS002005
- 907 Choi, Y.-S., Ho, C.-H., Park, C.-E., Storelvmo, T., & Tan, I. (2014). Influence of
 908 cloud phase composition on climate feedbacks. *Journal of Geophysical Re-
 909 search: Atmospheres*, *119*(7), 3687–3700. doi: 10.1002/2013JD020582
- 910 de Rosnay, P., Polcher, J., Bruen, M., & Laval, K. (2002). Impact of a physically
 911 based soil water flow and soil-plant interaction representation for modeling
 912 large-scale land surface processes. *Journal of Geophysical Research*, *107*(D11),
 913 4118. doi: 10.1029/2001JD000634
- 914 d’Orgeval, T., Polcher, J., & de Rosnay, P. (2008). Sensitivity of the West African
 915 hydrological cycle in ORCHIDEE to infiltration processes. *Hydrol. Earth Syst.
 916 Sci*, *12*, 1387–1401. doi: 10.5194/hess-12-1387-2008
- 917 Doutriaux-Boucher, M., & Quaas, J. (2004, March). Evaluation of cloud thermody-
 918 namic phase parametrizations in the LMDZ GCM by using POLDER satellite
 919 data. *Geophysical Research Letters*, *31*, 6126. doi: 10.1029/2003GL019095
- 920 Dufresne, J.-L., & Bony, S. (2008, Jan). An Assessment of the Primary Sources
 921 of Spread of Global Warming Estimates from Coupled Atmosphere Ocean
 922 Models. *Journal of Climate*, *21*(19), 5135. doi: 10.1175/2008JCLI2239.1
- 923 Duncan, D. I., & Eriksson, P. (2018, August). An update on global atmospheric ice
 924 estimates from satellite observations and reanalyses. *Atmospheric Chemistry &
 925 Physics*, *18*(15), 11205-11219. doi: 10.5194/acp-18-11205-2018
- 926 Ebert, E. E., & Curry, J. A. (1992, Mar). A Parameterization of Ice Cloud Opti-
 927 cal Properties for Climate Models. *Journal of Geophysical Research*, *97*(D4),

- 928 3831-3836. doi: 10.1029/91JD02472
- 929 Emanuel, K. A. (1991, November). A Scheme for Representing Cumulus Convection
930 in Large-Scale Models. *Journal of Atmospheric Sciences*, 48(21), 2313-2329.
931 doi: 10.1175/1520-0469(1991)048<2313:ASFRCC>2.0.CO;2
- 932 Emanuel, K. A., & Ivkovi-Rothman, M. (1999, Jun). Development and Evaluation of
933 a Convection Scheme for Use in Climate Models. *Journal of Atmospheric Sci-*
934 *ences*, 56(11), 1766-1782. doi: 10.1175/1520-0469(1999)056<1766:DAEOAC>2.0
935 .CO;2
- 936 Eyring, V., Bony, S., Meehl, G. A., Senior, C., Stevens, B., Stouffer, R. J., &
937 Taylor, K. E. (2015, Dec). Overview of the Coupled Model Intercom-
938 parison Project Phase 6 (CMIP6) experimental design and organisation.
939 *Geoscientific Model Development Discussions*, 8(12), 10539-10583. doi:
940 10.5194/gmdd-8-10539-2015
- 941 Fouquart, Y. (1988). Radiative transfer in climate models. In *Physically-based mod-*
942 *elling and simulation of climate and climatic change* (pp. 223–283). Springer.
- 943 Fouquart, Y., & Bonnel, B. (1980). Computations of solar heating of the earth’s
944 atmosphere- a new parameterization. *Beitraege zur Physik der Atmosphaere*,
945 53, 35–62.
- 946 Genthon, C., Piard, L., Vignon, E., Madeleine, J.-B., Casado, M., & Gallée, H.
947 (2017). Atmospheric moisture supersaturation in the near-surface atmosphere
948 at dome c, antarctic plateau. *Atmospheric Chemistry and Physics*, 17(1), 691–
949 704. Retrieved from <http://www.atmos-chem-phys.net/17/691/2017/> doi:
950 10.5194/acp-17-691-2017
- 951 Grandpeix, J.-Y., & Lafore, J.-P. (2010, Apr). A Density Current Parameteriza-
952 tion Coupled with Emanuel’s Convection Scheme. Part I: The Models. *Journal*
953 *of Atmospheric Sciences*, 67(4), 881-897. doi: 10.1175/2009JAS3044.1
- 954 Grandpeix, J.-Y., Lafore, J.-P., & Cheruy, F. (2010, Apr). A Density Current
955 Parameterization Coupled with Emanuel’s Convection Scheme. Part II:
956 1D Simulations. *Journal of Atmospheric Sciences*, 67(4), 898-922. doi:
957 10.1175/2009JAS3045.1
- 958 Grandpeix, J. Y., Phillips, V., & Tailleux, R. (2004, Oct). Improved mixing repre-
959 sentation in Emanuel’s convection scheme. *Quarterly Journal of the Royal Me-*
960 *teorological Society*, 130(604), 3207-3222. doi: 10.1256/qj.03.144

- 961 Heymsfield, A. J. (1977, February). Precipitation Development in Stratiform Ice
 962 Clouds: A Microphysical and Dynamical Study. *Journal of Atmospheric Sci-*
 963 *ences*, *34*, 367-381. doi: 10.1175/1520-0469(1977)034<0367:PDISIC>2.0.CO;2
- 964 Heymsfield, A. J. (1986, Apr). Ice Particles Observed in a Cirriform Cloud at -83°C
 965 and Implications for Polar Stratospheric Clouds. *Journal of Atmospheric Sci-*
 966 *ences*, *43*(8), 851-856. doi: 10.1175/1520-0469(1986)043<0851:IPOIAC>2.0.CO;
 967 2
- 968 Heymsfield, A. J., & Donner, L. J. (1990, August). A Scheme for Parameterizing
 969 Ice-Cloud Water Content in General Circulation Models. *Journal of Atmo-*
 970 *spheric Sciences*, *47*, 1865-1877. doi: 10.1175/1520-0469(1990)047<1865:
 971 ASFPIC>2.0.CO;2
- 972 Hogan, R. J., & Illingworth, A. J. (2000, Oct). Deriving cloud overlap statistics from
 973 radar. *Quarterly Journal of the Royal Meteorological Society*, *126*(569), 2903-
 974 2909. doi: 10.1002/qj.49712656914
- 975 Hourdin, F., Couvreux, F., & Menut, L. (2002, March). Parameterization of
 976 the Dry Convective Boundary Layer Based on a Mass Flux Representa-
 977 tion of Thermals. *Journal of Atmospheric Sciences*, *59*(6), 1105-1123. doi:
 978 10.1175/1520-0469(2002)059<1105:POTDCB>2.0.CO;2
- 979 Hourdin, F., Foujols, M.-A., Codron, F., Guemas, V., Dufresne, J.-L., Bony, S., ...
 980 Bopp, L. (2013, May). Impact of the LMDZ atmospheric grid configuration
 981 on the climate and sensitivity of the IPSL-CM5A coupled model. *Climate*
 982 *Dynamics*, *40*(9-10), 2167-2192. doi: 10.1007/s00382-012-1411-3
- 983 Hourdin, F., Grandpeix, J.-Y., Rio, C., Bony, S., Jam, A., Cheruy, F., ... Roehrig,
 984 R. (2013, May). LMDZ5B: the atmospheric component of the IPSL climate
 985 model with revisited parameterizations for clouds and convection. *Climate*
 986 *Dynamics*, *40*, 2193-2222. doi: 10.1007/s00382-012-1343-y
- 987 Hourdin, F., Jam, A., Rio, C., Couvreux, F., Sandu, I., Lefebvre, M.-P., ... Idelkadi,
 988 A. (2019, Sep). Unified Parameterization of Convective Boundary Layer Trans-
 989 port and Clouds With the Thermal Plume Model. *Journal of Advances in*
 990 *Modeling Earth Systems*, *11*(9), 2910-2933. doi: 10.1029/2019MS001666
- 991 Hourdin, F., Mauritsen, T., Gettelman, A., Golaz, J.-C., Balaji, V., Duan, Q., ...
 992 Williamson, D. (2017, Mar). The Art and Science of Climate Model Tun-
 993 ing. *Bulletin of the American Meteorological Society*, *98*(3), 589-602. doi:

- 994 10.1175/BAMS-D-15-00135.1
- 995 Hourdin, F., Musat, I., Bony, S., Braconnot, P., Codron, F., Dufresne, J.-L., ...
 996 Lott, F. (2006, Dec). The LMDZ4 general circulation model: climate perfor-
 997 mance and sensitivity to parametrized physics with emphasis on tropical con-
 998 vection. *Climate Dynamics*, 27(7-8), 787-813. doi: 10.1007/s00382-006-0158-0
- 999 Hourdin, F., Rio, C., Grandpeix, J.-Y., Madeleine, J.-B., Cheruy, F., Rochetin, N.,
 1000 ... Ghattas, J. (2020). LMDZ6A: the atmospheric component of the IPSL
 1001 climate model with improved and better tuned physics. *Journal of Advances in*
 1002 *Modeling Earth Systems*, e2019MS001892. doi: 10.1029/2019MS001892
- 1003 Iacobellis, S. F., & Somerville, R. C. (2000). Implications of microphysics for cloud-
 1004 radiation parameterizations: Lessons from TOGA COARE. *Journal of the*
 1005 *atmospheric sciences*, 57(2), 161–183. doi: 10.1175/1520-0469(2000)057<0161:
 1006 IOMFCR>2.0.CO;2
- 1007 Jam, A., Hourdin, F., Rio, C., & Couvreux, F. (2013, June). Resolved Versus
 1008 Parametrized Boundary-Layer Plumes. Part III: Derivation of a Statistical
 1009 Scheme for Cumulus Clouds. *Boundary-Layer Meteorology*, 147, 421-441. doi:
 1010 10.1007/s10546-012-9789-3
- 1011 Jouhaud, J., Dufresne, J. L., Madeleine, J. B., Hourdin, F., Couvreux, F., Ville-
 1012 franque, N., & Jam, A. (2018, Nov). Accounting for Vertical Subgrid-
 1013 Scale Heterogeneity in Low-Level Cloud Fraction Parameterizations. *Jour-*
 1014 *nal of Advances in Modeling Earth Systems*, 10(11), 2686-2705. doi:
 1015 10.1029/2018MS001379
- 1016 King, M. D., Platnick, S., Menzel, W. P., Ackerman, S. A., & Hubanks, P. A. (2013,
 1017 Jul). Spatial and Temporal Distribution of Clouds Observed by MODIS On-
 1018 board the Terra and Aqua Satellites. *IEEE Transactions on Geoscience and*
 1019 *Remote Sensing*, 51(7), 3826-3852. doi: 10.1109/TGRS.2012.2227333
- 1020 Klemp, J. B., & Wilhelmson, R. B. (1978, June). The Simulation of Three-
 1021 Dimensional Convective Storm Dynamics. *Journal of Atmospheric Sciences*,
 1022 35, 1070-1096. doi: 10.1175/1520-0469(1978)035<1070:TSOTDC>2.0.CO;2
- 1023 Konsta, D., Dufresne, J. L., Chepfer, H., Idelkadi, A., & Cesana, G. (2016, Aug).
 1024 Use of A-train satellite observations (CALIPSO-PARASOL) to evaluate trop-
 1025 ical cloud properties in the LMDZ5 GCM. *Climate Dynamics*, 47(3-4), 1263-
 1026 1284. doi: 10.1007/s00382-015-2900-y

- 1027 Laval, K., Le Treut, H., & Sadourny, R. (1981, Jan). Effect of cumulus parameter-
 1028 ization on the dynamics of a general circulation model. *Geophysical and Astro-*
 1029 *physical Fluid Dynamics*, 17(1), 113-127. doi: 10.1080/03091928108243676
- 1030 Lemonnier, F., Madeleine, J. B., Claud, C., Palerme, C., Genthon, C., L'Ecuyer,
 1031 T., & Wood, N. B. (2020, January). CloudSat-Inferred Vertical Structure
 1032 of Snowfall Over the Antarctic Continent. *Journal of Geophysical Research*
 1033 *(Atmospheres)*, 125(2), e31399. doi: 10.1029/2019JD031399
- 1034 Le Treut, H., & Li, Z. X. (1991). Sensitivity of an atmospheric general circula-
 1035 tion model to prescribed SST changes: Feedback effects associated with the
 1036 simulation of cloud optical properties. *Climate Dynamics*, 5, 175-187. doi:
 1037 10.1007/BF00251808
- 1038 Li, Z.-X. (1999, Apr). Ensemble Atmospheric GCM Simulation of Climate Interan-
 1039 nual Variability from 1979 to 1994. *Journal of Climate*, 12(4), 986-1001. doi:
 1040 10.1175/1520-0442(1999)012<0986:EAGSOC>2.0.CO;2
- 1041 Liou, K. (2002). *An Introduction to Atmospheric Radiation*. Academic Press.
- 1042 Loeb, N. G., Wielicki, B. A., Doelling, D. R., Smith, G. L., Keyes, D. F., Kato,
 1043 S., ... Wong, T. (2009, Jan). Toward Optimal Closure of the Earth's Top-
 1044 of-Atmosphere Radiation Budget. *Journal of Climate*, 22(3), 748. doi:
 1045 10.1175/2008JCLI2637.1
- 1046 Lurton, T., Balkanski, Y., Bastrikov, V., Bekki, S., Bopp, L., Brockmann, P., ...
 1047 Boucher, O. (2020). *Implementation of the CMIP6 forcing data in the IPSL-*
 1048 *CM6A-LR model*. (Submitted to JAMES) doi: 2019MS001940
- 1049 Mauritsen, T., Stevens, B., Roeckner, E., Crueger, T., Esch, M., Giorgetta, M.,
 1050 ... Tomassini, L. (2012, Mar). Tuning the climate of a global model.
 1051 *Journal of Advances in Modeling Earth Systems*, 4(3), M00A01. doi:
 1052 10.1029/2012MS000154
- 1053 McCoy, D. T., Tan, I., Hartmann, D. L., Zelinka, M. D., & Storelvmo, T. (2016,
 1054 Jun). On the relationships among cloud cover, mixed-phase partitioning, and
 1055 planetary albedo in GCMs. *Journal of Advances in Modeling Earth Systems*,
 1056 8(2), 650-668. doi: 10.1002/2015MS000589
- 1057 Mlawer, E. J., Taubman, S. J., Brown, P. D., Iacono, M. J., & Clough, S. A. (1997,
 1058 Jul). Radiative transfer for inhomogeneous atmospheres: RRTM, a vali-
 1059 dated correlated-k model for the longwave. *Journal of Geophysical Research*,

- 1060 102(D14), 16,663-16,682. doi: 10.1029/97JD00237
- 1061 Morcrette, J.-J. (1991, May). Radiation and cloud radiative properties in the Euro-
 1062 pean Centre for Medium Range Weather Forecasts forecasting system. *Journal*
 1063 *of Geophysical Research*, 96(D5), 9121-9132. doi: 10.1029/89JD01597
- 1064 Morcrette, J.-J., & Fouquart, Y. (1986, Feb). The Overlapping of Cloud Layers
 1065 in Shortwave Radiation Parameterizations. *Journal of Atmospheric Sciences*,
 1066 43(4), 321-328. doi: 10.1175/1520-0469(1986)043<0321:TOOCLI>2.0.CO;2
- 1067 Nam, C., Bony, S., Dufresne, J. L., & Chepfer, H. (2012, November). The ‘too few,
 1068 too bright’ tropical low-cloud problem in CMIP5 models. *Geophysical Research*
 1069 *Letters*, 39(21), L21801. doi: 10.1029/2012GL053421
- 1070 O’Dell, C. W., Wentz, F. J., & Bennartz, R. (2008, January). Cloud Liquid Wa-
 1071 ter Path from Satellite-Based Passive Microwave Observations: A New Cli-
 1072 matology over the Global Oceans. *Journal of Climate*, 21(8), 1721. doi:
 1073 10.1175/2007JCLI1958.1
- 1074 Rio, C., Del Genio, A. D., & Hourdin, F. (2019, April). Ongoing Breakthroughs in
 1075 Convective Parameterization. *Current Climate Change Reports*, 5(2), 95–111.
 1076 doi: 10.1007/s40641-019-00127-w
- 1077 Rio, C., & Hourdin, F. (2008, Feb). A Thermal Plume Model for the Convective
 1078 Boundary Layer: Representation of Cumulus Clouds. *Journal of Atmospheric*
 1079 *Sciences*, 65(2), 407-425. doi: 10.1175/2007JAS2256.1
- 1080 Rochetin, N., Grandpeix, J.-Y., Rio, C., & Couvreux, F. (2014, Feb). Deep Con-
 1081 vection Triggering by Boundary Layer Thermals. Part II: Stochastic Triggering
 1082 Parameterization for the LMDZ GCM. *Journal of Atmospheric Sciences*,
 1083 71(2), 515-538. doi: 10.1175/JAS-D-12-0337.1
- 1084 Sadourny, R. (1975, Nov). Compressible Model Flows on the Sphere. *Journal of At-*
 1085 *mospheric Sciences*, 32(11), 2103-2110. doi: 10.1175/1520-0469(1975)032<2103:
 1086 CMFOTS>2.0.CO;2
- 1087 Sadourny, R., & Laval, K. (1983). January and july performance of the lmd gcm.
 1088 *New Perspectives in Climate Modelling*, 71.
- 1089 Schlesinger, M. E., Oh, J.-H., & Rosenfeld, D. (1988, Oct). A Parameterization of
 1090 the Evaporation of Rainfall. *Monthly Weather Review*, 116(10), 1887. doi: 10
 1091 .1175/1520-0493(1988)116<1887:APOTEO>2.0.CO;2
- 1092 Smith, E. A., & Shi, L. (1992, May). Surface Forcing of the Infrared Cooling Profile

- 1093 over the Tibetan Plateau. Part I: Influence of Relative Longwave Radiative
 1094 Heating at High Altitude. *Journal of Atmospheric Sciences*, *49*(10), 805-822.
 1095 doi: 10.1175/1520-0469(1992)049<0805:SFOTIC>2.0.CO;2
- 1096 Sulak, A., Calabrese, W., Ryan, S. D., & Heus, T. (2020). The contributions of
 1097 shear and turbulence to cloud overlap for cumulus clouds. *Journal of Geophys-*
 1098 *ical Research: Atmospheres*, e2019JD032017. doi: 10.1029/2019JD032017
- 1099 Teixeira, J., Cardoso, S., Bonazzola, M., Cole, J., Delgenio, A., Demott, C., ...
 1100 Zhao, M. (2011, October). Tropical and Subtropical Cloud Transitions in
 1101 Weather and Climate Prediction Models: The GCSS/WGNE Pacific Cross-
 1102 Section Intercomparison (GPCI). *Journal of Climate*, *24*(20), 5223-5256. doi:
 1103 10.1175/2011JCLI3672.1
- 1104 Vial, J., Dufresne, J.-L., & Bony, S. (2013, Dec). On the interpretation of inter-
 1105 model spread in CMIP5 climate sensitivity estimates. *Climate Dynamics*,
 1106 *41*(11-12), 3339-3362. doi: 10.1007/s00382-013-1725-9
- 1107 Vignon, E., Hourdin, F., Genthon, C., Gallée, H., Bazile, E., Lefebvre, M.-P., ...
 1108 Van de Wiel, B. J. H. (2017, Jul). Antarctic boundary layer parametrization
 1109 in a general circulation model: 1-D simulations facing summer observations at
 1110 Dome C. *Journal of Geophysical Research (Atmospheres)*, *122*(13), 6818-6843.
 1111 doi: 10.1002/2017JD026802
- 1112 Webb, M., Senior, C., Bony, S., & Morcrette, J. J. (2001, Jan). Combining ERBE
 1113 and ISCCP data to assess clouds in the Hadley Centre, ECMWF and LMD
 1114 atmospheric climate models. *Climate Dynamics*, *17*(12), 905-922. doi:
 1115 10.1007/s003820100157
- 1116 Xie, S., Lin, W., Rasch, P. J., Ma, P.-L., Neale, R., Larson, V. E., ... Zhang, Y.
 1117 (2018, October). Understanding Cloud and Convective Characteristics in
 1118 Version 1 of the E3SM Atmosphere Model. *Journal of Advances in Modeling*
 1119 *Earth Systems*, *10*(10), 2618-2644. doi: 10.1029/2018MS001350
- 1120 Yamada, T. (1983, Jan). Simulations of Nocturnal Drainage Flows by a q^2 Turbu-
 1121 lence Closure Model. *Journal of Atmospheric Sciences*, *40*(1), 91-106. doi: 10
 1122 .1175/1520-0469(1983)040<0091:SONDFB>2.0.CO;2